Statistical properties of seismicity of fault zones at different evolutionary stages

G. Hillers,[1,]* P. M. Mai,[1] Y. Ben-Zion[2] and J.-P. Ampuero[1]

[1]*Institute of Geophysics, ETH Zurich, Zurich, Switzerland*
[2]*Department of Earth Sciences, University of Southern California, Los Angeles, USA*

SUMMARY

We perform a systematic parameter space study of the seismic response of a large fault with different levels of heterogeneity, using a 3-D elastic framework within the continuum limit. The fault is governed by rate-and-state friction and simulations are performed for model realizations with frictional and large scale properties characterized by different ranges of size scales. We use a number of seismicity and stress functions to characterize different types of seismic responses and test the correlation between hypocenter locations and the employed distributions of model parameters. The simulated hypocenters are found to correlate significantly with small L values of the rate-and-state friction. The final sizes of earthquakes are correlated with physical properties at their nucleation sites. The obtained stacked scaling relations are overall self-similar and have good correspondence with properties of natural earthquakes.

Key words: crustal deformation, dynamics, earthquakes, fault model, seismicity.

1 INTRODUCTION

A large number of multi-disciplinary observations and various theoretical frameworks, summarized by Ben-Zion & Sammis (2003), indicate that faults evolve toward structural simplicity and increasing regularity of the associated seismic response (e.g. Tchalenko 1970; Wesnousky 1994; Stirling *et al.* 1996; Lyakhovsky *et al.* 2001). Immature fault zones are formed as highly disordered structures associated with wide range of size scales and short correlation lengths of structural features. However, continuing deformation leads to progressive regularization manifested by coalescence, reduction in the range of size scales of fault irregularities, and development of larger correlation lengths (Ben-Zion & Sammis 2003, and references therein). Observational and theoretical studies indicate that geometrical heterogeneity plays a dominant role in the seismic response of a fault (e.g. Wesnousky 1994; Ben-Zion 1996; Zöller *et al.* 2005b). Disordered structures at early deformation phases like the San Jacinto fault appear to produce seismicity patterns that can be described, like regional seismicity, by power-law relations. On the other hand, mature localized structures like the San Andreas and the North Anatolian faults appear to produce more regular patterns associated with some periodicities.

In this work we perform a parameter space study of the seismic response of structures at different evolutionary stages, represented by different spatial distributions of the critical slip distance L in the rate-and-state (RS) friction framework. The employed distributions

attempt to characterize the fault maturity with an effective range of size scales composed of the following parameters: The microscopic range of size scales reflecting the degree of variability of local frictional properties, and the macroscopic range of size scales representing large scale structural properties. Our parameter space study examines systematically the response of model realizations associated with different sets of those parameters using a number of seismicity and stress response functions.

The empirical RS friction law used in this study was shown to be a powerful tool in modelling various stages of the seismic cycle, including pre-seismic slip and nucleation, the growth of dynamic instabilities, healing of fault surfaces, earthquake afterslip, aftershocks, and long deformation histories (Tse & Rice 1986; Rice 1993; Dieterich 1992, 1994; Ben-Zion & Rice 1995; Marone 1998; Rubin & Ampuero 2005). Previous studies of spatio-temporal evolution of slip on planar fault representations governed by RS friction (e.g. Rice 1993; Tullis 1996; Ben-Zion & Rice 1997; Lapusta *et al.* 2000) employed frictional properties corresponding to fairly homogeneous faults, where the only types of heterogeneities were lab-based depth-variations of the parameters a and b, and normal stress. More recently Liu & Rice (2005) and Hillers *et al.* (2006) used, respectively, spatial variations of a, b, and the critical slip distance L, to account for heterogeneous physical properties based on assumed temperature or structural variations of subduction or strike-slip fault zones. The physical basis for variations of the critical slip distance in natural fault structures is associated with the observations that L is correlated with the width of the gouge zone (Marone 1998, and references therein) and with the dominant wavelength that characterizes the roughness of sliding surfaces (Ohnaka 2003, and references therein). The available observations indicate that the

*Now at: the Institute for Crustal Studies, University of California, Santa Barbara, USA. E-mail: gregor@crustal.ucsb.edu
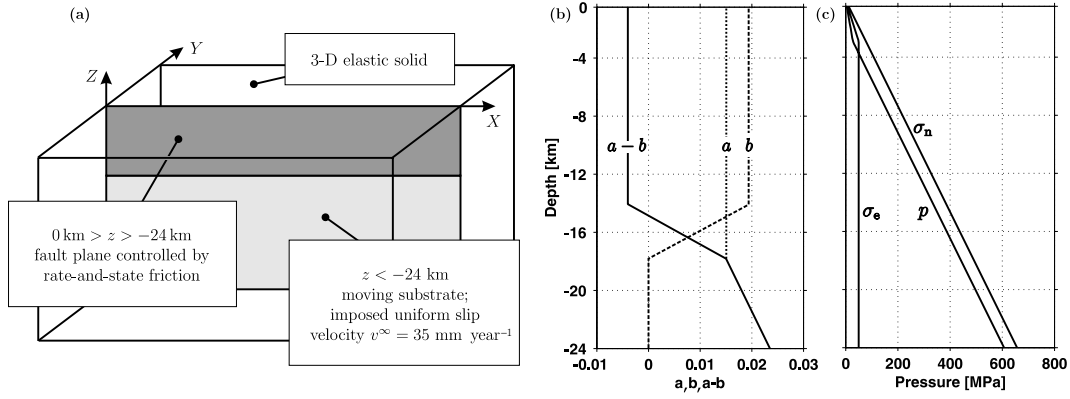
Figure 1. (a) Rate-and-state controlled vertical strike-slip fault plane embedded in a 3-D elastic half space, loaded by aseismic slip rate $v^\infty = 35$ mm year^{-1} at its downward extension. Frictional properties apply over a depth range of $Z_{\text{depth}} = 24$ km along a fault of length $X_{\text{length}} = [100, 200]$ km. (b) Employed profiles of frictional parameters, a, b and $a - b$. Standard distribution without velocity-strengthening zone at shallow depth. (c) Pressure profiles. Lithostatic normal stress, σ_{n}, pore pressure, p, and effective normal stress, σ_{e}.

width of the gouge zone in the brittle crust decreases with depth (Sylvester 1988; Chester & Chester 1998; Ben-Zion *et al.* 2003b) and that the roughness of sliding surfaces depends on the observation scale (Perfettini *et al.* 2003) and cumulative slip (Ben-Zion & Sammis 2003).

Motivated by the above field, laboratory and theoretical studies, we investigate the response characteristics of fault zones with different degrees of maturity using correlated 2-D L distributions. More specifically, we explore the effective range of size scales parametrized by the generated L distributions. The frictional microscopic range of size scales (R^{mic}) is defined by the effective range of L values, within limits controlled by computational constraints. The macroscopic range of size scales (R^{mac}), representing structural complexity, is specified by correlation lengths in the 2-D L maps and by the Hurst exponent. Using the algorithm of Hillers *et al.* (2006), designed to efficiently model geometrical and frictional properties on a planar 2-D fault geometry, we aim to isolate the relative importance among the different parameters. In agreement with previous results of Ben-Zion (1996), Ben-Zion *et al.* (2003a), Zöller *et al.* (2005b) and Hillers *et al.* (2006), we find that the effective range of size scales, characterizing the interdependence of frictional and structural properties, is the most effective parameter. In addition, comparisons of results to those of related work by Hillers *et al.* (2006) suggest that for equivalent ranges of microscopic size scales, topographic details of the 2-D L distribution control details of the seismicity pattern.

The remainder of the paper is organized as follows. We continue with a brief description of the numerical model, the governing equations and their implementation in the numerical scheme. In Section 3 we discuss some basic choices of frictional parameters and explain the generation of correlated 2-D distributions of the critical slip distance, L, parametrized as random-field models with properties governed by the above tuning parameters. Section 4 explains the compilation of a seismic catalogue and introduces physical quantities to describe the response of our simulations. Using these quantities, we discuss in Section 5 the effects of variations in the 2-D L parametrization (different correlation lengths along strike and downdip; changing Hurst exponent; different L value distributions) on the simulated seismicity. We then combine different correlation lengths in a set of hybrid models to represent fault zones with variable levels of heterogeneity. In Section 6, we introduce a testing procedure and then evaluate the dependence of hypocenter locations on physical properties at the site of the hypocenter. In Section 7, we explore

the effect of different binning strategies on the statistical evaluation, after which we discuss the magnitude dependence on physical quantities. Finally, we present scaling relations of observable quantities and discuss the overall applicability of our approach.

2 MODELLING PROCEDURE

We use the numerical model discussed by Hillers *et al.* (2006), who adopted the model geometry displayed in Fig. 1(a) from Rice (1993), Ben-Zion & Rice (1995, 1997) and Lapusta *et al.* (2000). Using the Dieterich–Ruina description of the rate-and-state evolution of the friction coefficient, the resulting set of governing first order differential equations is

$$\frac{\partial \theta(x, z, t)}{\partial t} = 1 - \frac{v(x, z, t)\,\theta(x, z, t)}{L(x, z)}$$

$$\frac{\partial v(x, z, t)}{\partial t} = \left(\frac{\dot{\tau}^{\text{r}}(x, z, t)}{\sigma_{\text{e}}(z)} - \frac{b(z)\,\dot{\theta}(x, z, t)}{\theta(x, z, t)} \right)$$

$$\times \left(\frac{\eta}{\sigma_{\text{e}}(z)} + \frac{a(z)}{v(x, z, t)} \right)^{-1}. \qquad (1)$$

The state variable θ evolves according to the 'slowness' or 'aging' form of the law, and L is a characteristic length scale over which a new population of contacts between two surfaces evolves. Using index notation (Hillers *et al.* 2006), the change of shear stress can be written as a convolution of the slip deficit field with the elastostatic kernel K

$$\tau_{ij}^{\text{r}}(t) = \sum_{k=1}^{nx} \sum_{l=1}^{nz} K_{|i-k|,j,l}\,(v^\infty t - u_{kl}(t)). \qquad (2)$$

The effective normal stress is denoted by σ_{e}, $\eta = f_\eta \cdot \eta_0$—with η_0 equal to the rigidity over two times the shear wave velocity—is the effective seismic radiation damping parameter, and a and b are temperature dependent frictional parameters relating changes in slip rate and state to frictional strength (Fig. 1b). The shear stress on the fault is computed using

$$\tau_{ij}(t) = \tau^0 + \tau_{ij}^{\text{r}}(t) - v_{ij}(t)\,\eta. \qquad (3)$$

with $\tau^0 = 100$ MPa (Hillers & Miller 2007).

We solve eqs (1) plus $\dot{u} = v$ using an explicit Runge-Kutta method with adaptive step-size control, DOP853 (Hairer *et al.* 1993), and the Fast Fourier Transform (FFT) is applied to evaluate eq. (2) (Rice 1993; Stuart & Tullis 1995; Rice & Ben-Zion 1996). For details of

the numerical procedure and specific solver parameters see Hillers (2006). Simulations of a 1500 year period seismicity on a 200 km long fault, discretized into 1024×128 computational cells, take between 7 and 15 days on a 2 GHz Linux workstation, depending on the particular response pattern.

We note that $f_\eta = 10^4$ used in this study does not bias our conclusions. This value is used because it significantly reduces the computational time for models generating mostly system-wide events. We compared the obtained statistics to a test case with $f_\eta = 1$, and found that the results are robust with the used spatio-temporal resolution.

3 PARAMETER SETTING

3.1 Nucleation size

To solve the problem in the continuum limit it is necessary to prevent discrete cells from failing independently of neighbouring cells. This is guaranteed if their size h is a small fraction of a critical size h^n (Rice 1993; Lapusta *et al.* 2000):

$$h_{R93}^n = \xi \cdot \frac{GL}{\sigma_e \, (b-a)_{max}}. \tag{4}$$

The geometrical factor ξ depends on the aspect ratio q of the cell. Here $q = 0.96$ and $\xi = 1.02$, estimated using the self-stiffness of a cell. The cell size is controlled by the minimum of $h_{R93}^n (x, z)$ over the fault plane, which in our models (Fig. 1b) scales with $\min[L(x,z)] = L_{min}$. This places strong constraints on computational efficiency, since the cpu time scales with the grid size. Thus, calculating slip histories within the continuum framework can be done at present only for values of L chosen to be one to two orders of magnitudes larger than laboratory values. With typical values from our study at seismogenic depth, $a = 0.015$, $b = 0.019$, $G = 30$ GPa and $\sigma_e = 50$ MPa, we obtain $h_{R93}^n = 765$ m and $h/h_{R93}^n = 0.25$ in regions where $L = L_{min} = 5$ mm, but a much better resolution in most parts of the fault. However, this criterion is not always sufficient to ensure proper resolution of the smallest scale features of slip. Another scale, which should be well resolved, is the smallest size of a slip localization zone reached during nucleation (Dieterich 1992; Rubin & Ampuero 2005, further discussed in the Appendix):

$$h_{D92}^n = 2.76 \cdot \frac{GL}{b \, \sigma_e}. \tag{5}$$

Although this has not been emphasized in the literature, for $a/b > 1 - \xi/2.76$ this length leads to a more stringent constraint on h than the condition based on h_{R93}^n. Here $h_{D92}^n = 435$ m and $h/h_{D92}^n = 0.44$, which may place our simulations at the edge of resolution on locations where $L = L_{min}$.

3.2 Frictional scaling parameters

Following the discussion in Hillers *et al.* (2006), we employ a modified $a - b$ profile that differs from a standard depth profile suggested by the interpretation of data obtained by Blanpied *et al.* (1991). We keep a constant negative $a - b$ value from the surface to $z = -15$ km (Fig. 1b), promoting instabilities over the entire seismogenic width, whereas the standard profile has an additional velocity-strengthening ($a - b > 0$) region above $z = -3$ km. Our choice has the advantage that seismicity occuring in shallower parts of the fault is exclusively controlled by heterogeneities in the governing 2-D L distributions, which is the focus of this study, and is not influenced by depth-dependent heterogeneities of the $a - b$ profile.

3.3 Correlated 2-D L distributions

The main focus of this study is to investigate seismic responses to 2-D L distributions that approximate physical properties of fault zones at different evolutionary stages. We represent different stages in the evolution of fault zones from structural disorder towards geometrical simplicity by variations in the effective range of size scales, i.e. we use variable microscopic ranges of L values (R^{mic}) together with different degrees of macroscopic fault zone segmentation, parametrized by characteristic length scales along-strike and down-dip (R^{mac}).

To generate heterogeneous 2-D fields of L values controlled by these tuning parameters, we use a spatial random field model, originally developed for characterizing slip distributions of large observed earthquakes (Mai & Beroza 2002). A spatial random field is characterized either in space by its auto-correlation function, $C(\mathbf{r})$, or in the spectral domain by its power spectral density, $P(\mathbf{k})$, where $\mathbf{k}$ is the wave number. In this study we apply the von Karman auto correlation function to model 2-D L distributions of variable degrees of heterogeneity. Its power spectral density is given as

$$P(\mathbf{k}) = \frac{4\pi \mathcal{H}}{K_{\mathcal{H}}(0)} \cdot \frac{a_x \cdot a_z}{(1 + \mathbf{k}^2)^{\mathcal{H}+1}} \tag{6}$$

with $\mathbf{k}^2 = a_x^2 \mathbf{k}_x^2 + a_z^2 \mathbf{k}_z^2$, the Hurst exponent, $\mathcal{H}$, and the modified Bessel function of the second kind (order $\mathcal{H}$), $K_{\mathcal{H}}$. The characteristic length scales in eq. (6) are the correlation length along-strike, a_x, and down-dip, a_z; the Hurst exponent describes the spectral decay at high wave numbers, and therefore partly controls the connectivity of L patches. Small values of $\mathcal{H}$ generate highly heterogeneous, disconnected maps, while values of $\mathcal{H}$ close to unity result in more continuous distributions. Strictly speaking, $\mathcal{H}$ is limited to the range $0 \le \mathcal{H} \le 1$; however, in one example we use a value of $\mathcal{H} = 1.2$ to show its effect on the seismic response more clearly. Fig. 2 illustrates random field examples for several correlation lengths, a_x and a_z, and constant Hurst exponent ($\mathcal{H} = 0.8$). Correlation lengths a_x in the range 1 km $\le a_x \le 100$ km are considered, with a main emphasis on models where 1 km $\le a_x = a_z \le 10$ km. Based on the chosen correlation lengths and Hurst exponent, we calculate the power spectral density $P(\mathbf{k})$ (eq. 6); the 2-D L function is obtained assuming a uniform-random phase in the interval $[-\pi \; \pi]$, applied to the 2-D inverse Fourier transformation. The 2-D inverse FFT is then carried out under the requirement of Hermitian symmetry to ensure a purely real-valued L distribution.

Our random field simulations use the spectral synthesis approach (Pardo-Iguzquiza & Chica-Olmo 1993), which generates a zero-mean Gaussian distribution with unit standard deviation considering all points on the 2-D plane. We rescale these fields such that the L values fall into the desired range of $-2.3 \le \log_{10}(L/m) \le -1$ (i.e. $L_{min} = 0.005$ m $\le L \le L_{max} = 0.1$ m). L_{min} is controlled by the continuum limit demand $h \ll h^n$, and L_{max} is required to make the nucleation size of the order of the seismogenic width of the fault. To achieve a uniform distribution of L values (Hillers *et al.* 2006), we resample the Gaussian distribution onto a uniform distribution in the range $[L_{min} \; L_{max}]$, illustrated in Fig. 2(g). Such cases have wide R^{mic}. The resulting spatial L distributions (Figs 2a–d) reflect this resampling approach by having larger regions of high and low L values, which also translates into steeper gradients of L (Fig. 3). Fig. 2(h) shows a Gaussian distribution of L values, centred around the mean value ($\log_{10}(L/m) = -1.65$), where small or large L values occur with smaller probability. Such cases have narrow R^{mic}. Correspondingly, the 2-D L maps (Figs 2e and f) are dominated
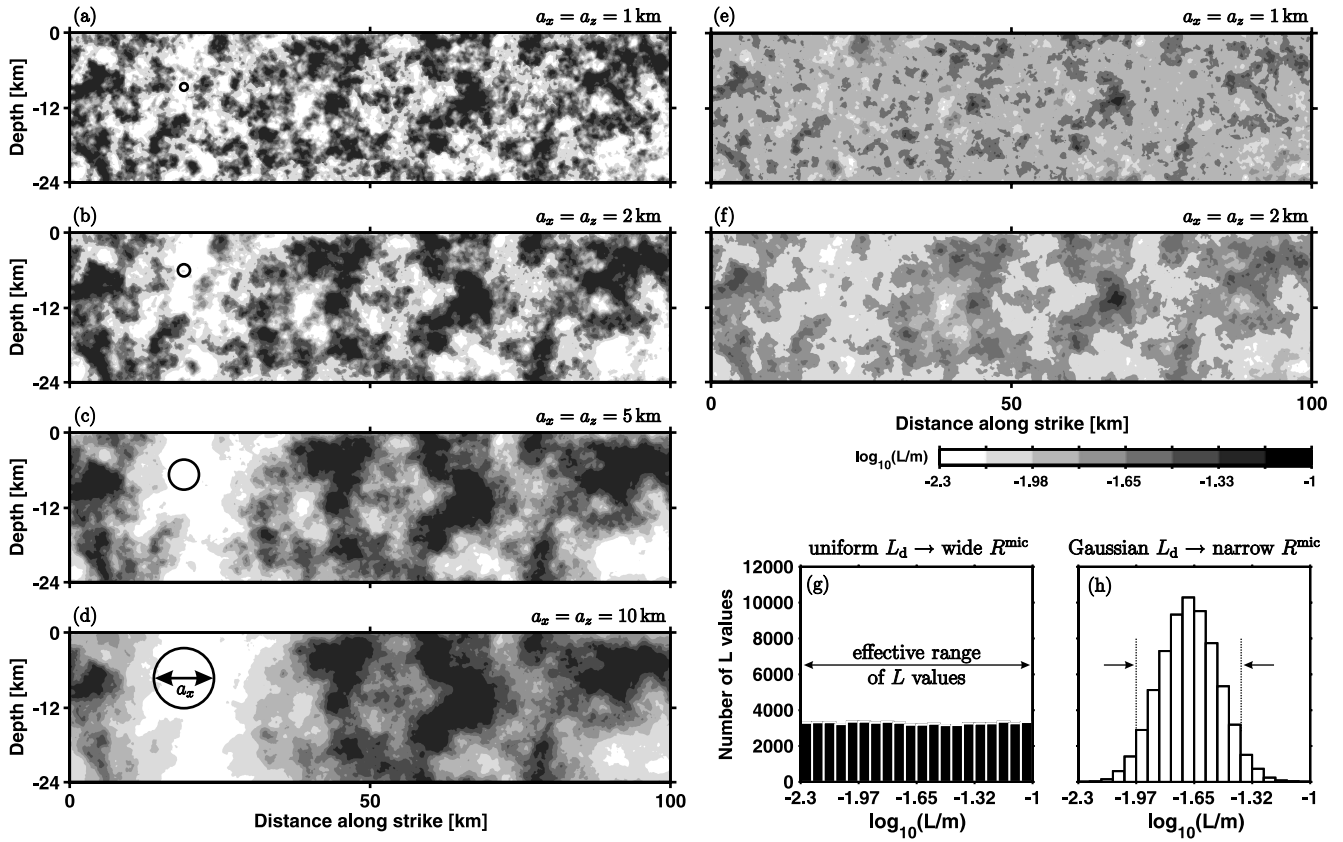
Figure 2. A typical set of correlated 2-D L distributions. The maps are generated using the same parameter set, i.e. same phase angle and Hurst exponent, $\mathcal{H} = 0.8$ (see Section 3). (a)–(d) Increase in correlation length along strike and depth, a_x and a_z, respectively, where values on the plane are distributed uniformly (L_d uniform $\rightarrow$ wide microscopic range of size scales, R^{mic}). (e) and (f) Spatial distributions of L values correspond to those in (a) and (b), with L_d Gaussian ($\rightarrow$ narrow R^{mic}). Corresponding horizontal profiles of the spatial L distributions are shown in Fig. 3. Histograms in (g) and (h) illustrate R^{mic}. They differ in the effective range of values of the parameter L, which is used to characterize different ranges of frictional size scales associated with fault zone maturity. The set of circles in (a)–(d) at $x = 20$ km illustrate the macroscopic range of size scales, R^{mac}, indicating a length scale over which structural properties change. The combined effect of R^{mic} with a particular sample of R^{mac} control the seismicity evolution of model simulations.

by grey areas, while the end-member values of high and low L—indicated by black and white, respectively—are poorly represented. The different topography of uniform and Gaussian distributed L values is also quantified in the corresponding standard deviations: $\sigma_{uniform} \approx 0.26$, while $\sigma_{Gauss.} \approx 0.11$, as well as in highly variable and strong gradients in case of the uniform L distribution. In the following we will use the abbreviation L_d to indicate distributions of L values across the 2-D L maps.

4 EARTHQUAKE PARAMETERS

4.1 Catalogue and stress functions

To compare seismicity of model faults with different sets of tuning parameters we determine several quantities from our simulations that are comparable to seismic observables listed in earthquake catalogues. We extract a seismic catalogue from the continuously simulated slip velocities generated by our numerical experiments using criteria for a seismic event introduced by Hillers *et al.* (2006). Cells are interpreted to be slipping seismically as long as the slip rates are larger than a certain velocity threshold, and the hypocenter is determined to be the cell that reached this threshold first (see Appendix). The algorithm measures the cumulative slip of a com-

pact zone of cells from the time when the hypocenter becomes unstable until all participating cells dropped below the threshold. The event size is measured by the scalar potency P (sum of seismic slip times rupture area in [km^2 cm]) associated with seismic slip (Ben-Zion 2003). The corresponding event magnitude M_L is obtained by the empirical quadratic scaling relation of Ben-Zion & Zhu (2002). The resulting earthquake catalogue is displayed and evaluated in common representation of frequency size (FS) statistics. Seismicity rate $r = N/t_s$ is determined by dividing the number of generated events, N, by the simulated time, t_s, neglecting initial quiescence whose duration depends on initial and boundary conditions. We follow Ben-Zion *et al.* (2003a) in calculating stress functions related to seismicity and criticality. In particular, we track the average stress, AS, and standard deviation of stress on the fault, SD, for $z > -15$ km to exclude minor stress variations in the velocity strengthening part at depth. In addition, we calculate spatial and average seismic coupling parameters $\chi(x, z)$ and $\bar{\chi}$ (for $z > -15$ km), respectively, to measure the partition of strain release between seismic and aseismic components

$$\chi(x, z, t) = \frac{u(x, z, t)_{seismic}}{u(x, z, t)_{total}}$$

$$\bar{\chi}(t) = \frac{\sum_x \sum_z u(x, z, t)_{seismic}}{\sum_x \sum_z u(x, z, t)_{total}}. \tag{7}$$
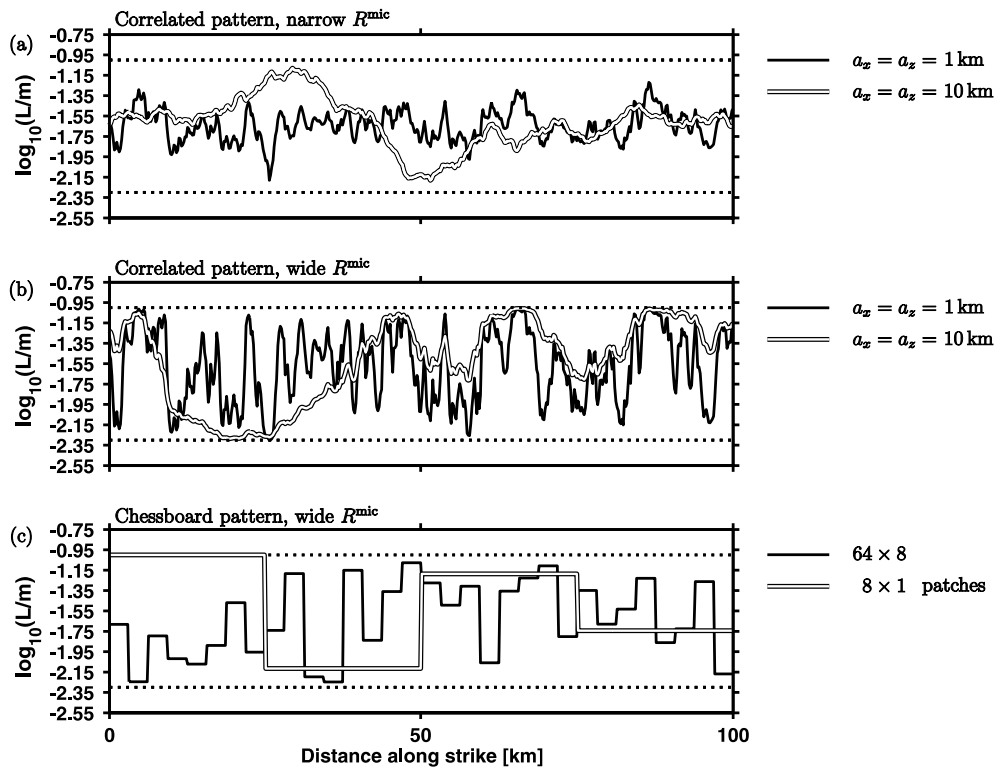
Figure 3. Horizontal profiles of 2-D L distributions at $z = -9$ km. (a) Correlated L distribution, L_d Gaussian ($\rightarrow$ narrow range of microscopic size scales), with $a_x = a_z = 1$ km and $a_x = a_z = 10$ km, respectively (Fig. 2e). (b) Correlated L distribution, L_d uniform ($\rightarrow$ wide R^{mic}), with $a_x = a_z = 1$ km and $a_x = a_z = 10$ km, respectively (Fig. 2a and d). (c) Example of a 2-D chessboard L distribution discussed in Hillers *et al.* (2006), L_d uniform ($\rightarrow$ wide R^{mic}), with 8 × 1 and 64 × 8 patches along strike and depth, respectively (Figs 9a and d in Hillers *et al.* 2006). Topography differences between (b) and (c) explain changes in response types between models sharing the same tuning parameter 'range of microscopic size scales'.

In principle, $a < b$ conditions applied over the entire fault width allow unstable slip everywhere, for all L. However, large nucleation zones of sizes comparable to the seismogenic width in regions with large L produce low fractions of coseismic slip on certain portions of the fault (see Fig. 7 in Hillers *et al.* 2006). Hence, some χ, $\bar{\chi}$ values discussed later are unrealistically low; however, this does not affect the tendencies and statistical features of the discussed results.

5 STATISTICAL PROPERTIES

5.1 Variable correlation lengths

5.1.1 General response

In a first set of simulations we focus on different response types of a set of eight models with variable correlation lengths a_x, a_z, using $a_x = a_z = [1, 2, 5, 10]$ km (Table 1, Group I). The set is divided into two times four models with wide and narrow distributed L values across the fault plane (Fig. 2, wide and narrow R^{mic}), respectively. Figs 4(a)–(d) summarizes results obtained from models with identical a_x, a_z, $\mathcal{H}$ but different ranges of L values. As illustrated by the black histograms (wide R^{mic}), small correlation lengths ($a_x = a_z = [1, 2]$ km) lead to preferred nucleation in regions where L is small. The corresponding FS statistics show relatively good agreement with the reference slope of the Gutenberg–Richter (GR) law characterizing seismicity of global strike-slip events shallower than 50 km (Frohlich & Davis 1993). This parameterization represents

fault zones with geometrical disorder leading to GR statistics over almost the entire magnitude range. This behaviour is usually referred to as 'critical' (Klein 1993; Main 1996). However, the simulations generate quasi-cyclic behaviour of seismicity where periods of quiescence alternate with periods of clustered seismic activity, which is due to the relatively short along-strike dimension of the fault. The main difference between the seismicity patterns of Figs 4(a) and (b) is that periods of quiescence last longer for $a_x = a_z = 1$ km, which is due to larger stress drops associated with largest events, causing larger coupling coefficients (Table 1). This indicates that the small-scale connectivity of physical properties allows the growth of instabilities into large events.

The difference between $\bar{\chi}$ in CL017 and CL018 (Table 1) is negligible compared to the coupling values of the $a_x = a_z = [1, 2]$ km models with narrow distributed L, since these models release about four times as much slip seismically. This is associated with a small seismicity rate, r, reflecting the periodic repeat of very large characteristic earthquakes ($M_L \approx 7.5$) rupturing the entire fault length. Such state of the system may be called 'supercritical', where the elevated probability of system-wide events is promoted by 2-D L distributions having less pronounced small-scale heterogeneities (*cf.* Figs 2e and f). The FS statistics of the simulations using the narrow L distribution are consistent with the characteristic earthquake response pattern of relatively homogeneous fault zones having a narrow effective range of microscopic size scales. The tendency of hypocenter clustering around average $\log_{10}(L)$ values reflects the underlying Gaussian L distributions. A straightforward interpretation of this observation is that most parts of the fault are occupied by moderate $\log_{10}(L)$ values (*cf.* Figs 2e and f). Since the nucleation

Table 1. For all models: $L_{min} = 0.005$ m, $L_{max} = 0.1$ m, $h/h^n_{D92} = 0.4$ $Z_{depth} = 24$ km, $nz = 128$. Group specific invariant parameters are: Group I: $X_{length} = 100$ km, $nx = 512$, $f_\eta = 100$. Group II: $X_{length} = 100$ km, $nx = 512$, $f_\eta = 100$. Group III: $X_{length} = 100$ km, $nx = 512$, $f_\eta = 100$. Group IV: $X_{length} = 200$ km, $nx = 1024$, $f_\eta = 1$. Note that rates, r, of models with different X_{length} need to be normalized to be comparable.

Model Name	a_x [km]	a_z [km]	H	R^{mic}	t_s [years]	N	r	$\bar{\chi}$	Fig. No.
Group I — Variable a_x, a_z									
CL010	1	1	0.8	narrow	1780	136	0.08	0.81	4, 5, 3, 6, 11, 12, 14
CL009	2	2	0.8	narrow	1791	93	0.05	0.83	4, 5, 13
CL008	5	5	0.8	narrow	1295	83	0.06	0.61	4, 5
CL005	10	10	0.8	narrow	1299	94	0.07	0.63	4, 5, 3, 6, 11, 12, 14
CL017	1	1	0.8	wide	1284	535	0.42	0.27	4, 5, 3, 6, 11, 12, 14
CL018	2	2	0.8	wide	1297	565	0.43	0.18	4, 5, 13
CL019	5	5	0.8	wide	1327	160	0.12	0.22	4, 5
CL020	10	10	0.8	wide	1327	203	0.15	0.28	4, 5, 3, 6, 11, 12, 14
Group II — Variable a_x, Constant a_z									
CL004	20	10	0.8	narrow	695	47	0.07	0.40	7
CL002	50	10	0.8	narrow	629	57	0.09	0.49	7
CL003	100	10	0.8	narrow	710	54	0.08	0.45	7
Group III — Variable H									
CL013	1	1	0.5	narrow	1778	103	0.05	0.46	—
CL010	1	1	0.8	narrow	1780	136	0.08	0.81	—
CL014	1	1	1.2	narrow	1275	69	0.05	0.78	—
CL015	2	2	0.5	narrow	1783	68	0.04	0.82	—
CL009	2	2	0.8	narrow	1791	93	0.05	0.83	—
CL016	2	2	1.2	narrow	1781	65	0.04	0.76	—
CL011	5	5	0.5	narrow	1792	25	0.01	0.83	8
CL008	5	5	0.8	narrow	1295	83	0.06	0.61	8
CL012	5	5	1.2	narrow	1785	112	0.06	0.57	8
CL026	5	5	0.5	wide	803	278	0.35	0.48	8
CL019	5	5	0.8	wide	1327	160	0.12	0.22	8
CL022	5	5	1.2	wide	1325	287	0.22	0.40	8
Group IV — Hybrid Models									
CL024	var.	var.	0.8	narrow	797	106	0.13	0.49	9
CL023	var.	var.	0.8	wide	784	425	0.54	0.27	9

size scales with L, accelerating patches are relatively large and can not be arrested by sharp contrasts in the state variable or shear stress distribution because of the smooth spatial character of the governing L distribution (*cf.* Fig. 3a).

Sampling R^{mac} at its upper boundary, i.e. using larger correlation lengths ($a_x = a_z = [5, 10]$ km, Figs 4c and d), the pattern of the FS statistics changes for both narrow and wide L_d. In cases of wide R^{mic} we observe an increased tendency of earthquake nucleation towards sites with average L values. Interestingly, for an underlying narrow R^{mic} and $a_x = a_z = 10$ km, earthquakes tend to nucleate over the entire L interval. The slopes of the FS statistics are flattening, but show nevertheless approximate power-law behaviour or distributions over a large magnitude range for seismicity with $M_L <$ 7. Compared to this behaviour, large events occur with a reduced probability, indicating a 'subcritical' state of the system, where the largest events do not rupture the entire area of the model fault. This is due to large-scale structural heterogeneities that can stop the growth of instabilities (Fig. 2d, extended patches of similar L values at $x =$ [25, 60, 90] km). Despite the similarity between the FS distribution of both approaches, the size of largest earthquakes differs almost by one magnitude (at least for $a_x = a_z = 5$ km), leading to significant differences in seismic coupling. We conclude that for small correlation lengths and a constant Hurst exponent, the microscopic range of size scale is the most effective controlling parameter. Models with wide and narrow R^{mic} produce seismicity patterns associated with early stages of fault evolution and mature fault zones, respectively. For larger correlation lengths, however, the FS statistics and seismic-

ity of models with narrow distributed L values on the fault plane do not differ significantly from those of the wide L distribution. Hence, for relatively large a_x, a_z the macroscopic structure, i.e. spatially extended clusters of similar L values that represent segmentation of the model fault, controls the 2-D L distributions and associated seismic response (Table 2).

5.1.2 Temporal clustering

In Fig. 5 we plot the coefficient of variation of interevent times, CV, as a function of lower magnitude cut-off for narrow and wide R^{mic}, respectively. The parameter CV is defined as the ratio of the standard deviation and mean value of the interevent time distribution. The value $CV = 1$ corresponds to a random Poisson process, $CV > 1$ denotes temporally clustered seismicity, and $CV < 1$ represents (quasi-) periodic temporal activity. The results of Fig. 5(a) can be compared to the associated temporal seismicity evolution shown in Fig. 4, revealing the periodic repeat of large events for models with small correlation lengths and narrow R^{mic}. Larger CV at smaller values of the lower M_L cut-off indicate clustered activity for all correlation lengths, and for $a_x = a_z = [5, 10]$ km the temporal distributions are approximately random. For the wide R^{mic} model (Fig. 5b) earthquakes show a higher degree of clustering compared to the narrow R^{mic} model, most significantly for $a_x = a_z = [1, 2]$ km, which is also confirmed by the seismicity time evolution in Fig. 4. However, this strong clustering may be exaggerated by the overall cyclic seismicity generated by these models, which is due
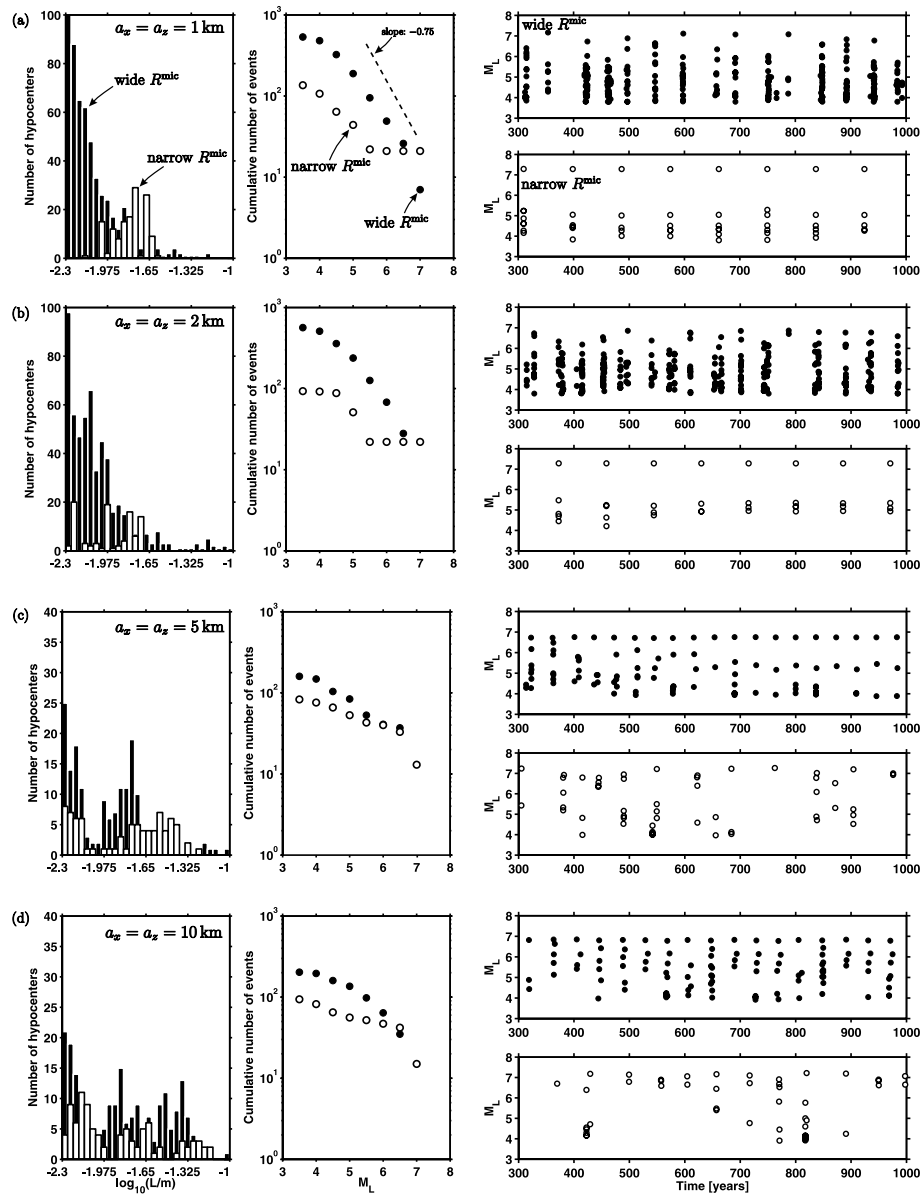
Figure 4. Statistics in response to 2-D *L* distributions with variable correlated lengths along strike and depth, $a_x = a_z =$ (a) 1 km, (b) 2 km, (c) 5 km, (d) 10 km (Fig. 2). Left panels: Distribution of hypocenters as a function of *L* at the hypocenter. Middle panels: FS statistics; dashed line shows a reference slope. Right panels: Temporal seismicity evolution. Black bars/solid circles: wide R^{mic}. White bars/open circles: narrow R^{mic}. For result classification see Table 2.

Table 2. FS denotes frequency-size distribution, ES the evolutionary state, SYS the system state and DF the dominating feature of the *L* parameterization. R^{mic} abbreviates 'microscopic range of size scales'. The macroscopic range of size scales is determined by the range of applied correlation lengths or the Hurst exponent. The distinction between 'Gutenberg-Richter' and 'approx. power law' refers to significant differences of the slopes of corresponding FS statistics.

| Parameterization		Short correlation lengths	Large correlation lengths
	FS:	characteristic	approx. power law
Gaussian L_{d}	ES:	mature	—
→ narrow R^{mic}	SYS:	supercritical	subcritical
	DF:	microscopic range of size scales	macroscopic segmentation
	FS:	Gutenberg-Richter	approx. power law
uniform L_{d}	ES:	immature	—
→ wide R^{mic}	SYS:	critical	subcritical
	DF:	microscopic range of size scales	macroscopic segmentation
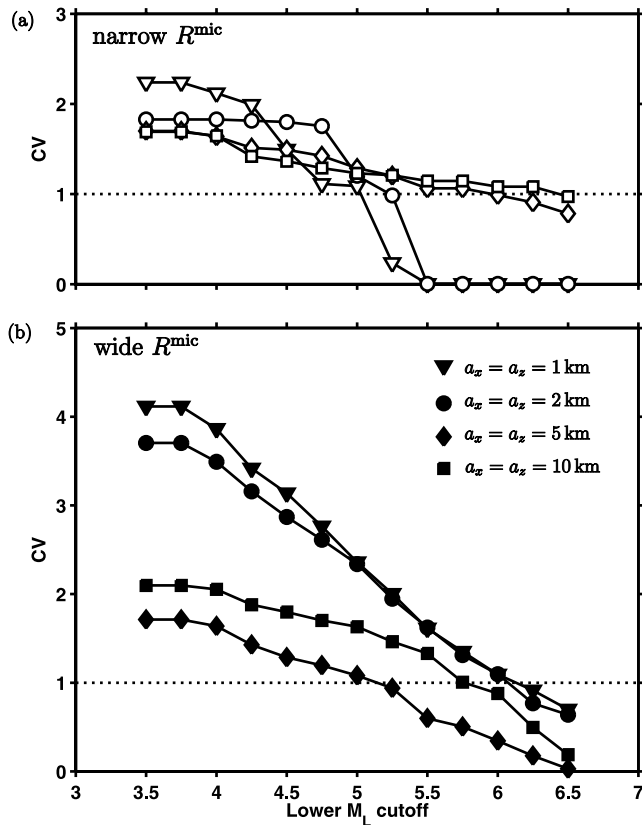
Figure 5. The coefficient of variation, *CV*, defined as the ratio of standard deviation and mean value of the interevent time distribution, as a function of lower magnitude cut-off. Large *CV* denote clustered activity as for the wide R^{mic} models with small correlation lengths. Low values of *CV* represent (quasi-) periodic seismicity as in the corresponding narrow R^{mic} models (Figs 4a and b, right column). $CV = 1$ indicates a random process.

to the short repeat distance along strike (100 km). The *CV* function shows an inverse linear dependence on the lower cut-off magnitude, which is expected as smaller and hence more events are included, but reflects nevertheless the properties of temporal clustering. In both cases, the short correlation length models show a steeper gradient of *CV* vs. M_L cut-off compared to cases where correlation lengths are longer, and reflects the efficiency of a_x and a_z as tuning parameters.

5.1.3 Stress functions

Fig. 6 illustrates the differences between models controlled by variable parameters in terms of the stress functions *AS* (average stress) and *SD* (standard deviation of stress) over the rupture plane. The average stress for models with short correlation length ($a_x = a_z = 1$ km) and narrow *L* distribution (open lines) reflects the corresponding seismicity evolution (Fig. 4). The stress functions show a regular pattern of largest amplitude fluctuations corresponding to the periodic repeat of a $M_L > 7$ event (Fig. 6a). Large correlation lengths ($a_x = a_z = 10$ km) lead to less regular but still quasi-periodic changes in *AS* and *SD*, where the amplitudes show a less regular behaviour compared to Fig. 6(a). Similar to the $a_x = a_z = 1$ km case, the quasi-periodic occurrence of $M_L > 7$ events controls the stress evolutions (*cf.* Fig. 4d). In contrast, the *AS* evolution for a uniform *L* distribution shows the most irregular occurrence of stress drops presented here (Figs 6c and d). For small a_x and a_z, significant stress drops

of variable amplitude correlate with the occurrence of large $M_L \approx$ 7 events (Fig. 6d), but are not equidistant in time. Longer correlation lengths lead to a more regular pattern with smaller amplitudes but higher frequency of $M_L \approx 7$ occurrence (Fig. 6d). Compared to cases with small correlation lengths, relatively small drops in *AS* are accompanied by relatively large deflections in the standard deviation. However, both functions in Figs 6(c) and (d) are not as heterogeneous as the output of the discrete model realizations of Ben-Zion *et al.* (2003a). This indicates that even realizations with small-scale geometrical *L* fluctuations (approximately random 2-D *L* pattern) solved in the continuum limit do not produce high critical-like stress fluctuations as discrete models do.

For distributions with a narrow range of *L* values the stress functions are more homogeneous than corresponding functions of models with wide *L* range. Note that the average stress levels of models with large correlation lengths are generally larger than those of the corresponding small-scale correlation simulations. This indicates that large a_x, a_z do not necessarily smooth the response type of these systems, in accordance with the corresponding FS statistics. Moreover, the average temporal stress levels for wide *L* distributions are larger than those of the narrow distributed values of the critical slip distance, indicating that a wide range of microscopic size scales leads to a state closer to criticality. This dependence is also seen in loading sequences of dynamical models with heterogeneous stress distributions (*J. Ripperger*, pers. comm.). The small-scale stress fluctuations from chessboard models with the largest degree of structural heterogeneity (64×8 patches along strike and depth) in Hillers *et al.* (2006) are larger than those of the case shown in Fig. 6(c). This is interpreted as a result of steeper topography in the 2-D *L* distribution of the chessboard models (Figs 3b and c), since the *L* gradients at patch boundaries are larger than *L* gradients in the present uniformly distributed *L* models. This shows that for models with an equally wide R^{mic}, differences in the 2-D *L* topography becomes a tuning parameter. The comparison of stress evolutions between Figs 6(a) and (b) and 6(c) and (d), and between Figs 6(a) and (c) and 6(b) and (d) highlights the differences in the effectivity of the tuning parameters R^{mac} and R^{mic}, as outlined above.

To summarize, the combined effects of the microscopic range of sizes scales, and different correlation lengths defining the macroscopic range of size scales, control the spatio temporal seismicity evolution (*cf.* Table 2). The effect of R^{mic} is most prominent at short correlation lengths, whereas for larger a_x, a_z the resulting large scale segmentation of *L* clusters controls the seismic response. In the employed model realizations, both R^{mac} and R^{mic} are limited by finite size effects such as cell size, *h*, width of the seismogenic zone, *W*, and fault length, X_{length}. The spatial dimension of a computational cell is about 200 m, which leads to an approximately random 2-D *L* distribution for small a_x, a_z. Larger correlation lengths are of the same order of magnitude as *W*, leading to the discussed segmentation of the fault regardless of specific L_d. Moreover, the fault length $X_{length} = 100$ km possibly influences the response statistics because of the periodic boundary conditions. Since *W* is fixed for physical reasons, we performed additional simulations using $L \in$ [0.0025 0.1] m and $h \approx 100$ m to increase R^{mic}, and simulations using $X_{length} = [200, 400]$ km with variable correlation lengths and wide and narrow R^{mic}. Without discussing results of these computationally demanding simulations in detail, we find that they support the conclusions presented here, in particular the robustness of the associated FS statistics. Observed differences in magnitude-time evolution are due to the increased model space, such as the blurring of cyclic seismicity, which leads to more realistic seismicity-time patterns.
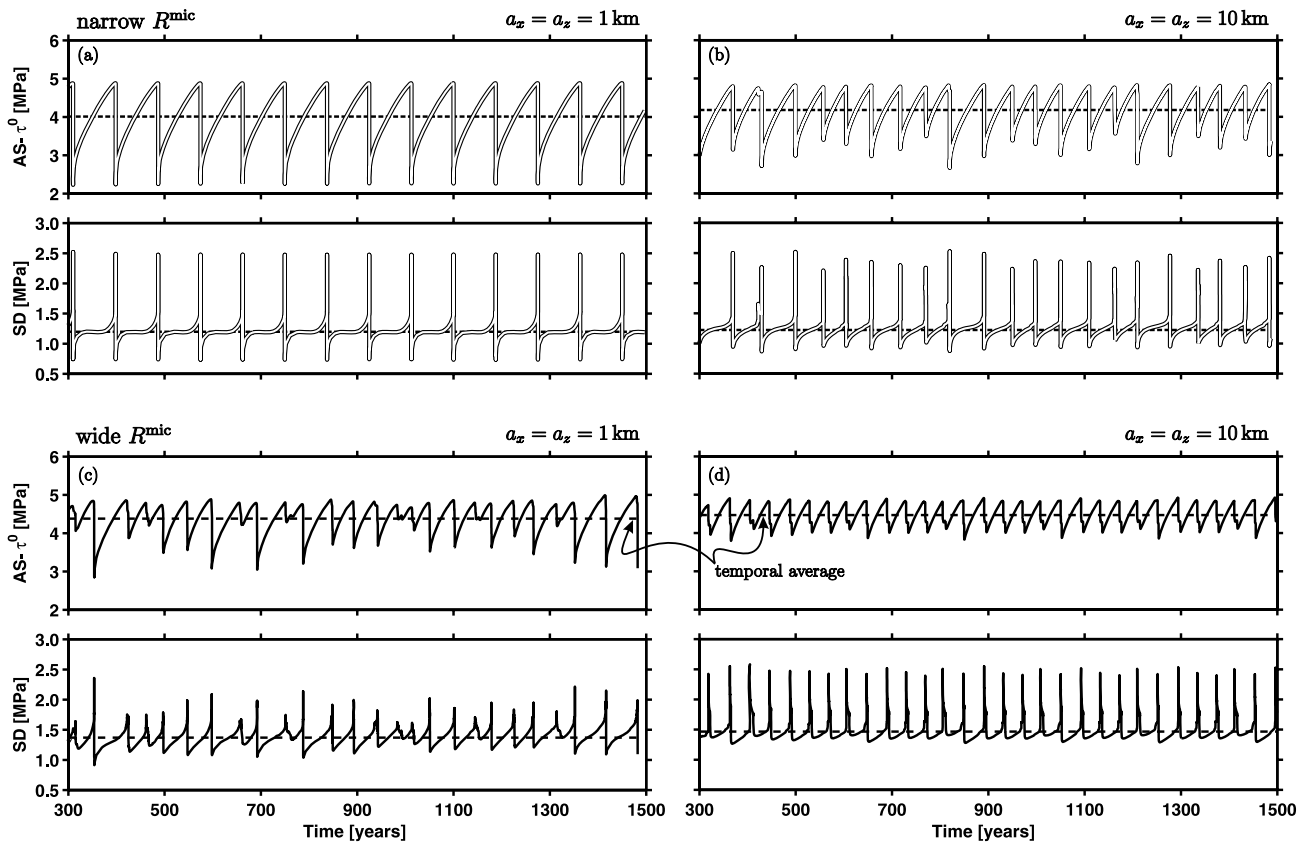
Figure 6. Average stress, *AS*, and its standard deviation, *SD*, in the top 15 km of the fault for models with short (a and c) and long (b and d) correlation lengths. The stress functions reflect temporal seismicity evolution of simulations shown in Fig. 4, right panel.
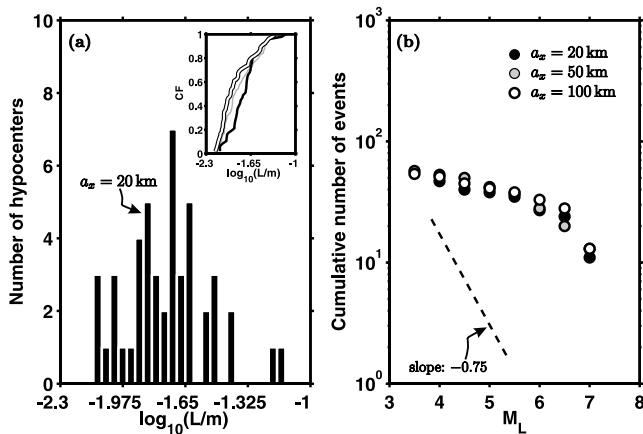

Figure 7. (a) Number of hypocenters as a function of L at hypocenter location for models with variable a_x and $a_z = 10$ km = const., $\mathcal{H} = 0.8 =$ const. The inset shows corresponding cumulative density functions to illustrate the similarity of the discussed results. Black line: $a_x = 20$ km. Grey line: $a_x = 50$ km. White line: $a_x = 100$ km. (b) FS statistics. Dashed line indicates reference slope. The three simulations produce very similar statistics, indicating that the correlation length along strike is no tuning parameter for $a_x > 10$ km.

5.2 Variable a_x, Constant a_z

Next we vary the correlation length along strike, a_x, while keeping $a_z = 10$ km = const., and use the narrow distribution of L values. (Table 1, Group II). Fig. 7(a) shows the number of hypocenters for the range of L values at the hypocenter location for $a_x = 20$ km.

The inset plots the corresponding cumulative frequency distribution for $a_x = [20, 50, 100]$ km. As in Fig. 4, the bell-shaped distribution of hypocenters as a function of L at the hypocenter reflects the underlying Gaussian L_d. The distribution of hypocenters is not very sensitive to the actual value of a_x as revealed by the similarity of the cumulative frequency distributions. The resulting FS statistics (Fig. 7b) confirm that the response is insensitive to changes in $a_x \geq 20$ km. The slope of the statistics indicates a relatively low ratio of small to large events, consistent with the observation made in models with $a_x = a_z = [5, 10]$ km. A relatively low seismicity rate, r, and large values for $\bar{\chi}$ (Table 1) indicate that the slip deficit is mainly released by a few large earthquakes, characteristic for the behaviour of relatively mature fault zones.

5.3 $\mathcal{H}$ as a tuning parameter

In the previous sections we used variable correlation lengths with a constant Hurst exponent to parametrize different degrees of structural heterogeneity. An alternative parametrization of macroscopic properties is to keep a_x, a_z constant and to vary $\mathcal{H}$. Figs 8(a)–(c) show three different realizations with $\mathcal{H} = [0.5, 0.8, 1.2]$, that lead to a corresponding increase in segmentation. Larger $\mathcal{H}$ values decrease the number but increase the size of connected patches occupied by similar L, using $a_x = a_z = 5$ km = const. and wide L distribution (note that $\mathcal{H} = 1.2$ is, strictly speaking, not admissible, but has been chosen for illustration purposes). The most significant difference revealed by the FS statistics (Figs 8d–f) between models with narrow and wide L distributions (open and solid circles), respectively, appears for $\mathcal{H} = 0.5$. Here, the narrow L model repeatedly produces a single $M_L = 7.0$ event rupturing the entire fault, whereas
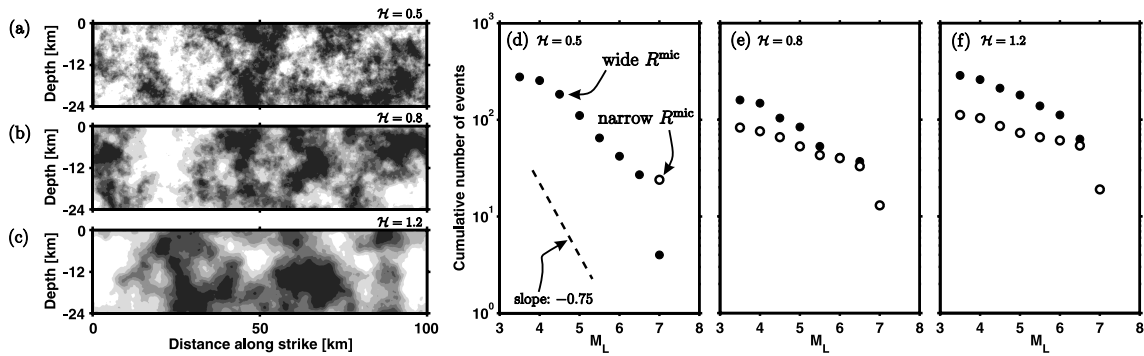
Figure 8. (a)−(c) 2-D L distributions for variable $\mathcal{H}$ and $a_x = a_z = 5$ km = const. to demonstrate the use of the Hurst exponent as a tuning parameter for roughness (wide R^{mic}; Colorrange as in Fig. 2). (d)–(f) Corresponding FS statistics. Dashed line: Reference slope.

the FS statistics of the wide L model shows an approximately GR behaviour over almost the entire magnitude range. For $\mathcal{H} = [0.8, 1.2]$ the differences between models with different ranges of L values are less significant having a relatively flat cumulative FS distribution. As revealed by values of the coupling coefficient $\bar{\chi}$ (Table 1, Group III), simulations with narrow R^{mic} produce more large events than corresponding distributions with wide R^{mic}. Comparing the results displayed in Figs 4 and 8, we find similarities in the behaviour of random-like and fragmented models generated with a_x, a_z variable, $\mathcal{H}$ constant and a_x, a_z constant, $\mathcal{H}$ variable, respectively. In agreement with previous findings, seismicity of models with small-scale spatial heterogeneity (small $\mathcal{H}$) is most effectively controlled by the microscopic range of size scales, whereas fragmented models (large $\mathcal{H}$) with different L_d tend to have more similar responses. This confirms that R^{mic} dominates the response for spatially very heterogeneous 2-D L distributions, whereas R^{mic} becomes less effective when the size of zones with similar L values are comparable to the seismogenic width. We tested two more sets with constant $a_x = a_z = [1, 2]$ km, and variable Hurst exponent (Table 1). These six simulations produce very similar response types compared to the model with $a_x = a_z = 2$ km and $\mathcal{H} = 0.8$ (Section 5.1). We detect no significant difference amongst the simulations (similar r, $\bar{\chi}$) indicating that the response is not sensitive to the Hurst exponent for correlation lengths less than five. In the following sections, we examine further models with variable correlation lengths and constant Hurst exponent.

5.4 Hybrid models

We discuss two hybrid models which are composed of 16 different areas along strike on a fault with $X_{\mathrm{length}} = 200$ km, each area being 24 km deep and 12.5 km long. Each patch contains a portion of a 2-D L distribution with different a_x and a_z, where pairs of a_x/a_z range from 1/1 km to 40/10 km, approximating variable degrees of structural heterogeneity along a fault. By comparing the results of two simulations with a narrow and wide L_d, respectively, to previously discussed behaviour related to constant correlation lengths, we can infer which section of the fault controls the seismic response. We find that regions of small correlation lengths dominate the seismic slip accumulation, indicated by the coupling coefficient $\chi(x, z, t)$ (not shown). This trend is also observable for the narrow L_d model, but less pronounced. Although the correspondence is significant, it might be biased by two factors. First, the transitions in L across area boundaries are more abrupt between areas of smaller a_x, a_z, which might lead to preferred nucleation because of stress concentrations. Second, areas with long correlation lengths are dominated

by large L values which tend to stabilize the slip response (*cf.* Fig. 7 in Hillers *et al.* 2006). This last aspect of the simulation represents one possible realization among a large number of similar models. Large L values could also be concentrated in small fault regions (i.e. be characterized by short correlation lengths), and hence would stabilize the system's response on a more local scale.

The histograms in Fig. 9(a) highlight differences in the response type between the two approaches. The model with wide L_d produces significantly higher seismicity rate, and hypocenters tend to nucleate in regions where L is small. The FS statistics show a steeper and hence more realistic slope compared to the narrow L_d model. The predominating occurrence of medium $\log_{10}(L)$ values and resulting smoothness of the state variable and shear stress leads to larger events ($M_L > 7$), as discussed for previous models. Significant difference between the two response types is also illustrated by the temporal seismicity evolution. The comparison of Figs 9(c) and (d) with Fig. 4 indicates that the response of the hybrid wide L_d model is similar to the models with short correlation lengths (Figs 4a and b). In contrast, the hybrid narrow L_d model generates seismicity which matches the behaviour of models with long correlation lengths (Figs 4c and d). The results are in agreement with those of Sections 5.1 and 5.3, confirming that different ranges of size scales dominate the characteristics of the model response. Specifically, the average stress for the case with a wide range of L values (Fig. 9e) is very heterogeneous, indicating a closer proximity to critical-like behaviour and higher correspondence with immature fault zones. The stress evolution of the model with narrow range of L values is more regular, and the largest stress drops associated with the occurrence of repeated $M_L > 7$ events correspond to the characteristic event response of more mature fault zones.

6 HYPOCENTER LOCATIONS

6.1 Testing procedure

A typical hypocenter distribution, taken from model CL018 (Table 1), is shown in Fig. 10(a). The non-random spatial distribution of hypocenter locations (*HL*) is a striking feature, hence we investigate its relation to the heterogeneous physical properties along the fault. The location of a hypocenter (centroid) is the outcome of the earthquake nucleation process. Relevant properties of nucleation under rate-and-state friction are reviewed in the Appendix. The ability of a fault patch to initiate an instability is primarily controlled by the ratio of two lengths: the patch size and the nucleation size. If the patch size is fixed, the amount of seismic release depends as well on this ratio. At any given fault location, the concept of a patch
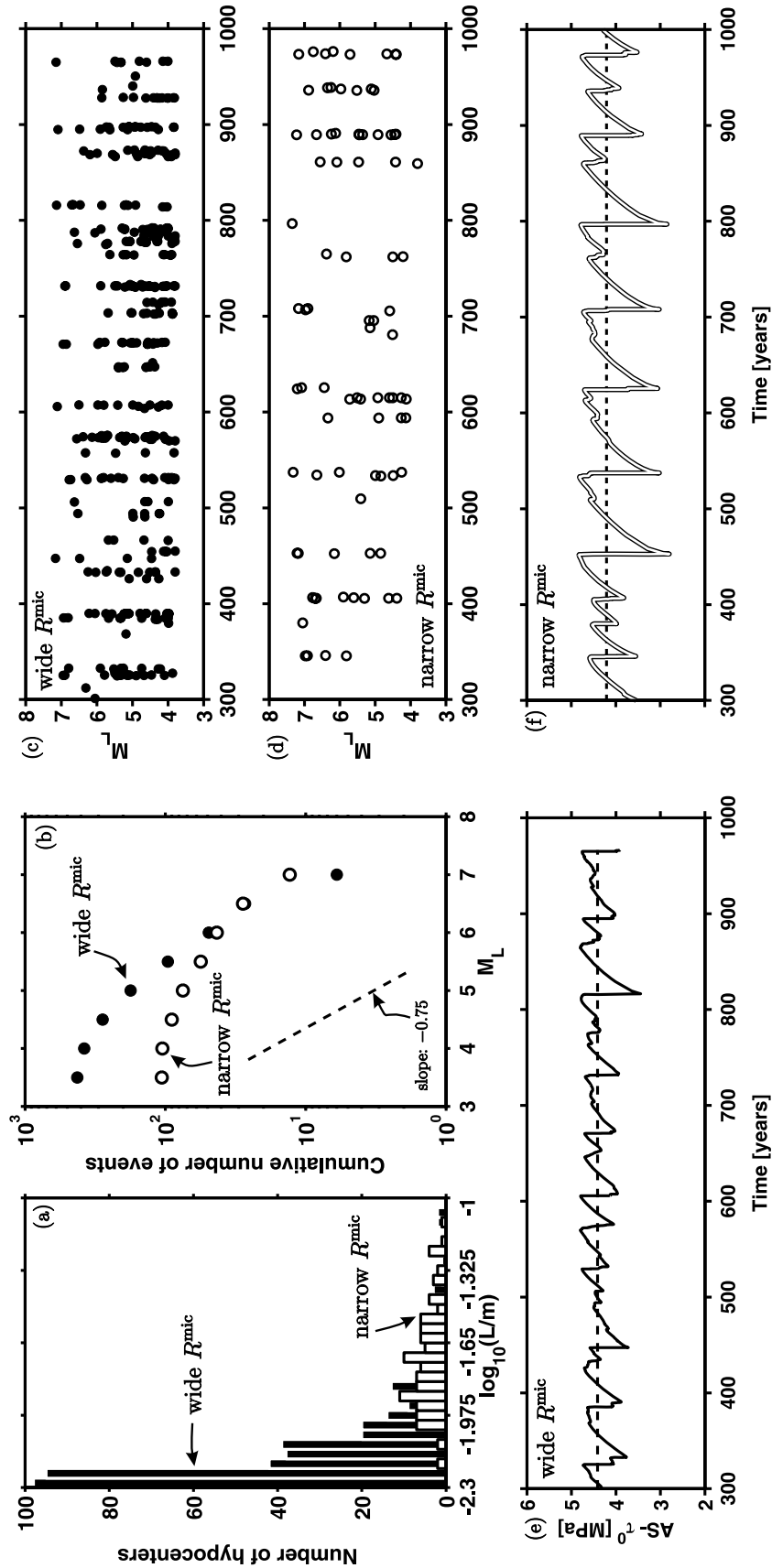
Figure 9. Results from two hybrid models. (a) Distribution of hypocenter locations as a function of *L* at the hypocenter. (b) Corresponding FS statistics. Dashed line: Reference slope. Seismicity evolution for (c) wide R^{mic} and (d) narrow R^{mic}. Average stress on the upper 15 km of the fault for (e) wide R^{mic} and (f) narrow R^{mic}.
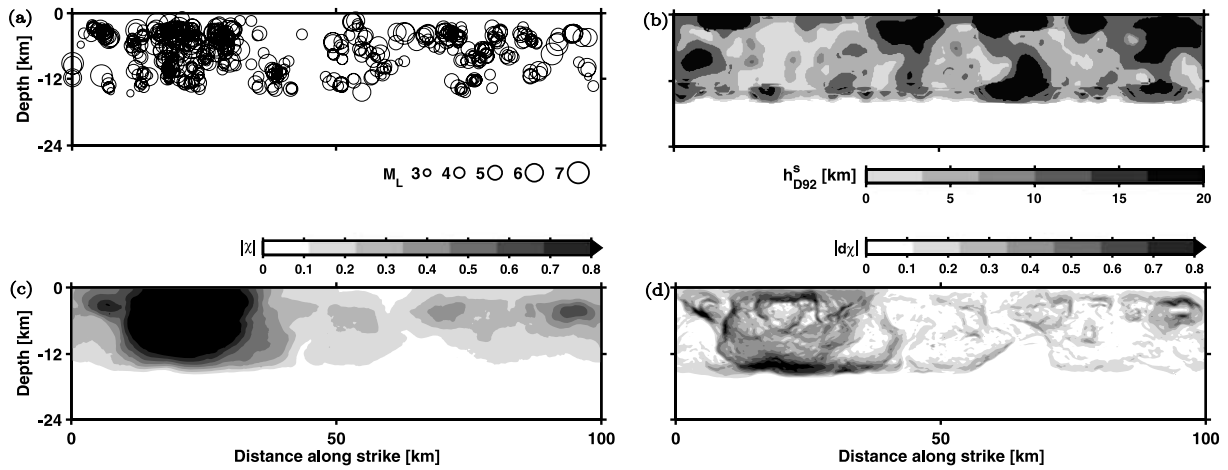
Figure 10. Example to illustrate the correlation procedure described in Section 6.2. (a) Hypocenter distribution of model CL018, $a_x = a_z = 2$ km, wide R^{mic}. (b) Effective nucleation size, h^s_{D92}, based on the estimate of h^n_{D92} in eq. (5). (c) Normalized spatial distribution of the coupling coefficient χ. (d) Normalized spatial derivative of χ, $d\chi$.
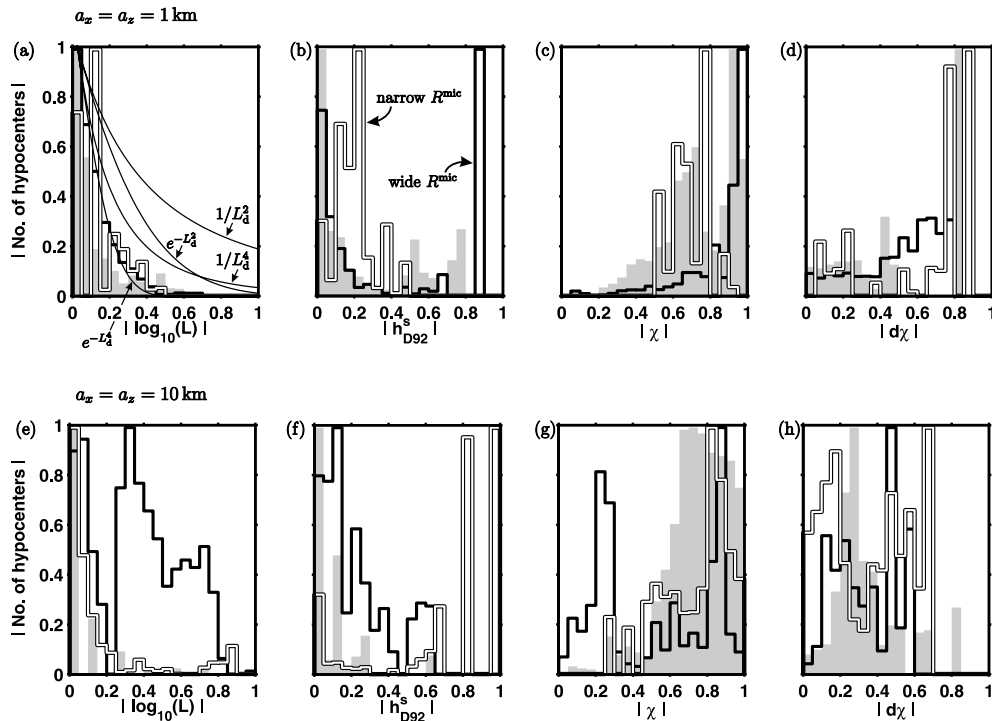

Figure 11. Correlation of hypocenter locations with physical parameters L, h^s_{D92}, χ, $d\chi$, normalized to the underlying distribution of corresponding values, scaled to the interval [0 1], for (a)−(d) $a_x = a_z = 1$ km, and (e)−(h) $a_x = a_z = 10$ km. White bars correspond to narrow R^{mic}, black bars to wide R^{mic}, and grey shaded bars to the chessboard models (top: 64 × 8; bottom: 8 × 1 patches) from Hillers *et al.* (2006). Note the relatively good correlation between the occurrence of hypocenter locations and small values of L, h^s_{D92} at the nucleation site.

size is mechanically related to the effective stiffness of the local loading conditions prevailing during nucleation. This depends on geometrical constraints on the size of a nucleation zone on the fault, which might be non-stationary across seismic cycles or contain a broad mixture of length scales. In contrast to the patch size, the nucleation size is an intrinsic property related to friction parameters and effective normal stress.

We compare hypocenter locations to the spatial distributions of parameters defined on the basis of the nucleation size as follows: To take into account the heterogeneity of $h^n = h^n_{D92}$ in the vicinity

of each site we tentatively define an effective nucleation size, h^s (x, z), as the local average of h^n over a circular region surrounding (x, z) (Fig. 10b). Since a/b and σ_e are uniform in most of the seismogenic region, the local value of the nucleation length h^n (x, z) is basically proportional to $L(x, z)$. The radius of the averaging region is set according to the following rationale. We hypothesize that nucleation starts at the scale of the effective nucleation length h^s and that the nucleation process tends to smooth heterogeneities of shorter scales. A consistent averaging scale to compute h^s is then h^s itself. This implicit definition is implemented such that we make
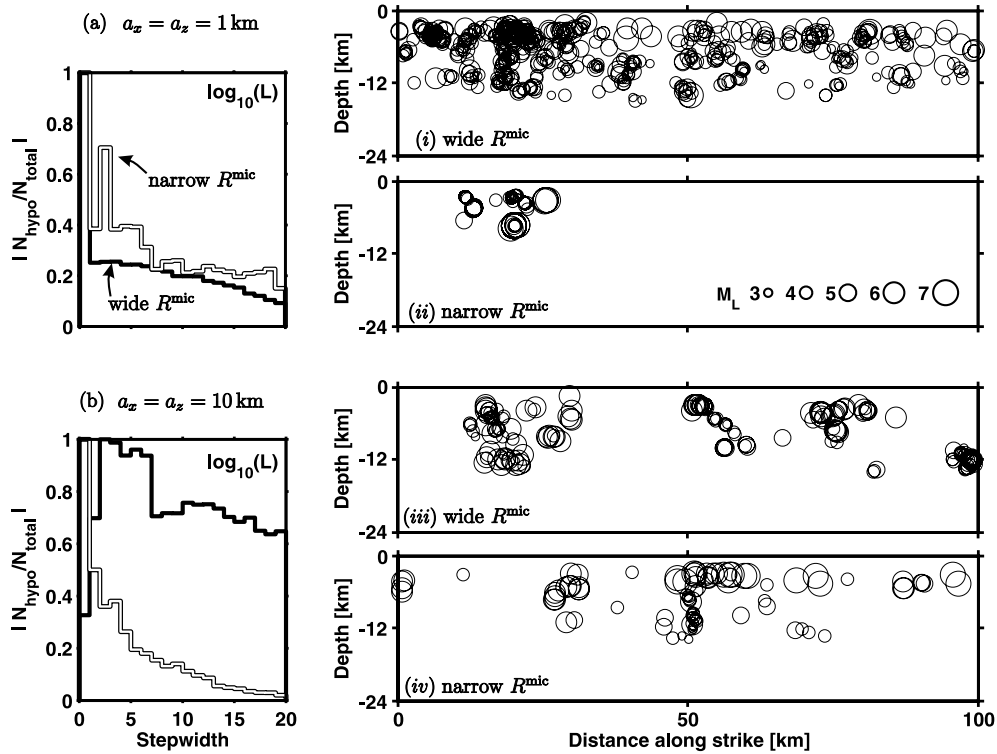
Figure 12. Spatial distribution of hypocenters for (a) $a_x = a_z = 1$ km and (b) $a_x = a_z = 10$ km. Left panels show the normalized number of cells containing a hypocenter in a certain L range, defined by the stepwidth of the normalized vector that contains sorted L values at which earthquakes nucleate. Right panel shows spatial distributions of hypocenters of corresponding models (i) CL017, (ii) CL010, (iii) CL020, (iv) CL005 (see Table 1). Models in (i)–(iii) have minimum L values around $x = 20$ km, (iv) at around $x = 50$ km, explaining the clustering of hypocenters at these locations. For details see text.

filtered versions $h^n(D)$ of the h^n map, with running averages over circular patches of diameter D. At each location (x, z), h^s is defined as the smallest D for which $h^n(D) = D$, i.e. the patch diameter that equals its locally averaged nucleation size.

Features of loading conditions that are persistent over the cycles can be mapped by the seismic coupling coefficient, χ (eq. 7; Fig. 10c). Moreover, as stress concentrations are expected at the boundaries between regions of high and low coupling, the norm of the gradient of χ, $d\chi$ (Fig. 10d), might indicate preferred sites for earthquake nucleation.

6.2 Dependence of hypocenter locations

6.2.1 Hypocenter frequency

A strategy to statistically assess which of the parameters L, h^s, χ and $d\chi$ correlates best with the *HL* requires a certain expectation or hypothesis to be tested (e.g. Schorlemmer *et al.* 2006; Woessner *et al.* 2006). However, such a statistical treatment is beyond the scope of the present study. Instead, we simply plot the number of hypocenters at sites with given parameter value, normalized by the number of occurrence of the parameter value (e.g. L_d), scaled to the interval [0 1]. Figs 11(a)–(h) show examples from each L_d with a short and large correlation length, respectively. We also plot results taken from Hillers *et al.* (2006) for comparison. The results may be summarized as follows:

(1) Correlating the *HL* with L at the hypocenter, we observe for models with $a_x = a_z = 1$ km (Fig. 11a) a characteristic functional dependence with a maximum at small values, followed by a decay

proportional to $1/L_d$, where L_d denotes the full range of L values. This suggests that once the distribution of size scales is known it has to be convolved with this function to estimate the overall occurrence of hypocenter locations. The same proportionality is observed for large correlation lengths and the narrow L_d, as well as the 8×1 chessboard model (Fig. 11e).

(2) The correlation of hypocenters with the effective nucleation size h^s_{D92} is similar to the $\log_{10}(L)$ dependence (Figs 11b and f). The significant signals at larger values are due to the correlation of *HL* with large h^s_{D92}, caused by the influence of larger h^n_{D92} values at the $a - b$ transition zone at depth. Neglecting this particular result, we observe that correlations of hypocenters with L and L-dependent parameters show the same trends.

(3) Regions of large coupling coefficients tend to have the most likely hypocenter locations (Figs 11c and g). However, it is difficult to conclude that earthquakes tend to nucleate in these regions because χ is large there. More likely, large χ depend on properties that promote nucleation in these areas. The peak at $a_x = a_z = 10$ km for L_d uniform reveals that a significant fraction of earthquakes can nucleate in regions of small coupling. The comparison of L- and h^s_{D92}-statistics to χ-statistics for small correlation lengths implies that regions of high coupling coincide with regions of small L values. This trend is also observable for large correlation lengths.

(4) Our original assumption that earthquakes nucleate preferably in regions between locked and creeping parts has not been confirmed unevoquially based on the correlations in Figs 11(d) and (h). We find a significant tradeoff between models having different ranges of size scales for small and large correlation lengths, respectively.
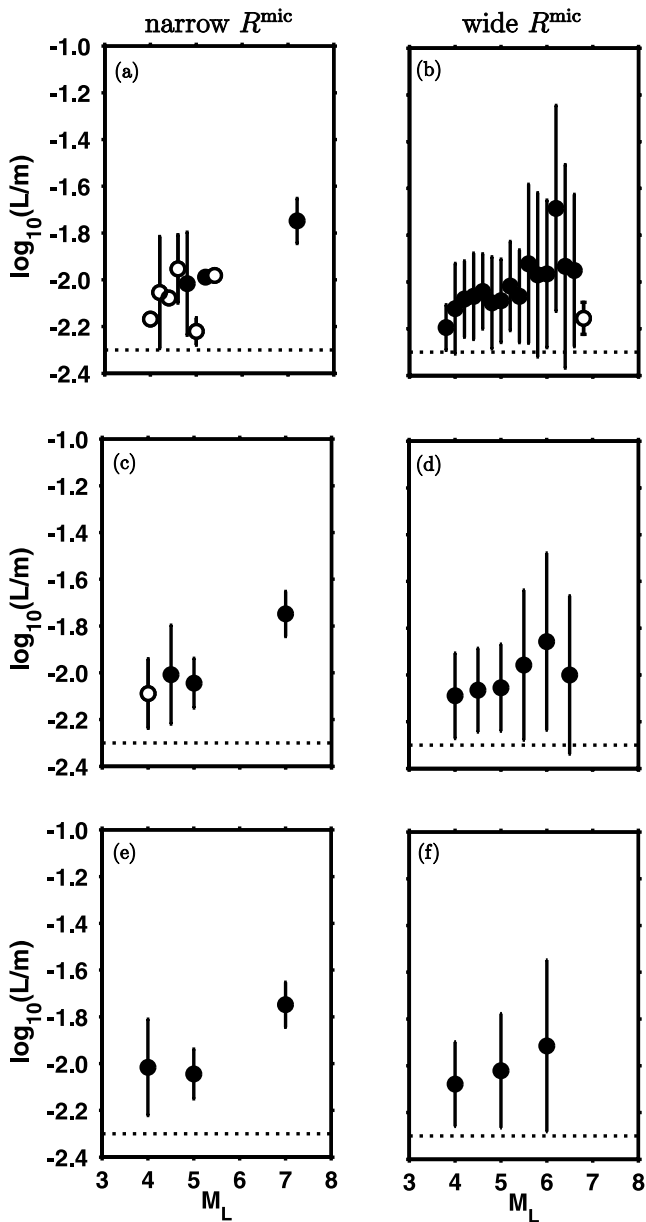
Figure 13. Average $\log_{10}(L)$ value at nucleation sites for different magnitude intervals, M_I. (a), (c) and (e) narrow R^{mic}, $N = 93$ (CL009). (b), (d) and (f) wide R^{mic}, $N = 565$ (CL018; see Table 1). For both models $a_x = a_z = 2$ km, $\mathcal{H} = 0.8$. Upper row: $M_I = 0.2$. Middle row: $M_I = 0.5$. Bottom row: $M_I = 1$. Solid circles represent data points determined with ≥ 10 events, open circles contain <10 events, and open circles without errorbar represent one single event. Dotted lines denote minimum L value, $L_{min} = 0.005$ m.

Results taken from the chessboard-type models (Hillers *et al.* 2006) that have a wide range of L values match those generated by the present models with a wide R^{mic} and small correlation lengths. However, for $a_x = a_z = 10$ km they tend to follow the same trends observed for models with a narrow microscopic range of size scales.

6.2.2 *Fraction of sites*

While the normalized hypocenter locations in Figs 11(a)–(h) provide a relative measure of how many events nucleate in a certain

Table 3. Results of linear regressions to data presented in Fig. 13. M_I: Magnitude interval or bin width. The slope of the linear regression is denoted by β, and R^2 is the correlation coefficient (0: no fit; 1: perfect fit).

Model	Sampling Threshold	$M_I = 0.2$ β	R^2	$M_I = 0.5$ β	R^2	$M_I = 1$ β	R^2
			Narrow R^{mic}				
CL009	1	0.11	0.60	0.11	0.93	0.10	0.83
	10	0.11	0.99	0.11	0.91	0.10	0.83
			Wide R^{mic}				
CL018	1	0.07	0.29	—	—	—	—
	10	0.10	0.60	0.07	0.52	0.08	0.97

parameter range (bin), the histograms in Figs 12(a) and (b) quantify the normalized number of hypocenter locations (cells) as a function of increasing L value range. In particular, the *x*-axis plots the increasing L value range in which hypocenters nucleate (i.e. $[L_{min} \; L_v]$, with $v = 1, N/20, 2N/20, \ldots, N$, where N is the total number of events per simulation). The *y*-axis shows the number of sites (cells) in the increasing $[L_{min} \; L_v]$ range that contain a hypocenter, normalized by the total number of cells occupied by values in that range, N_{total}. Large values of N_{hypo}/N_{total} at small v suggest that many cells within that $[L_{min} \; L_v]$ range act as hypocenters, i.e. many sites with a small L value become hypocenters. In contrast, larger ratios at larger v indicate a less localized nucleation process, where only a few sites with small L values act as hypocenters. There, physical properties of a larger scale control the growth of instabilities.

Panels *i–iv* in Fig. 12 show the spatial distributions of hypocenter locations for wide and narrow L_d, respectively. For small a_x, a_z (panels *i*, *ii*), the hypocenters are spread over the whole fault plane if L_d is wide, but are spatially constrained for narrow L_d. This can be understood by the spatial distribution of the smallest L values across the fault. Common to all models is that most earthquakes nucleate around the along-strike position $x = 20$ km where the L values are smallest (Fig. 2). This particularity is controlled by the phase-angle distribution in the random field generation, but not picked deliberately, i.e. the position of high and low L values is not a tuning parameter since it is a relative position because of periodic boundary conditions. For large a_x, a_z (panels *iii*, *iv*) we observe an inverse behaviour compared to *i* and *ii*. For wide L_d, the hypocenters become more localized, whereas for narrow L_d they are more spread. However, the distributions in *iii* and *iv* are similar, confirming the dominant role of fault segmentation parametrized by large correlation lengths. These findings illustrate the controlling character of the combined effects of micro- and macroscopic properties and their relative efficiency.

As can be seen in Figs 10(a) and 12, there is no dependence of event magnitude on nucleation depth. Large events can nucleate at shallow depth (Fig. 12 (*ii*), $x = 25$ km), as well as near the transition zone at about 14 km depth (Fig. 12 (*i*), $x = 50$ km). Similar observations are made for small events. This insensitivity to depth is due to the used $a - b$ profile without a transition at $z = 3$ km, a constant effective normal stress, and no particular depth dependence of the 2-D L distributions, although distributions accounting for the reduced width of the slip zone may be more realistic.

7 MAGNITUDE DEPENDENCE

7.1 Variable binning

In Section 6.2 we investigated hypocenter locations as a function of four spatially distributed physical parameters independent of
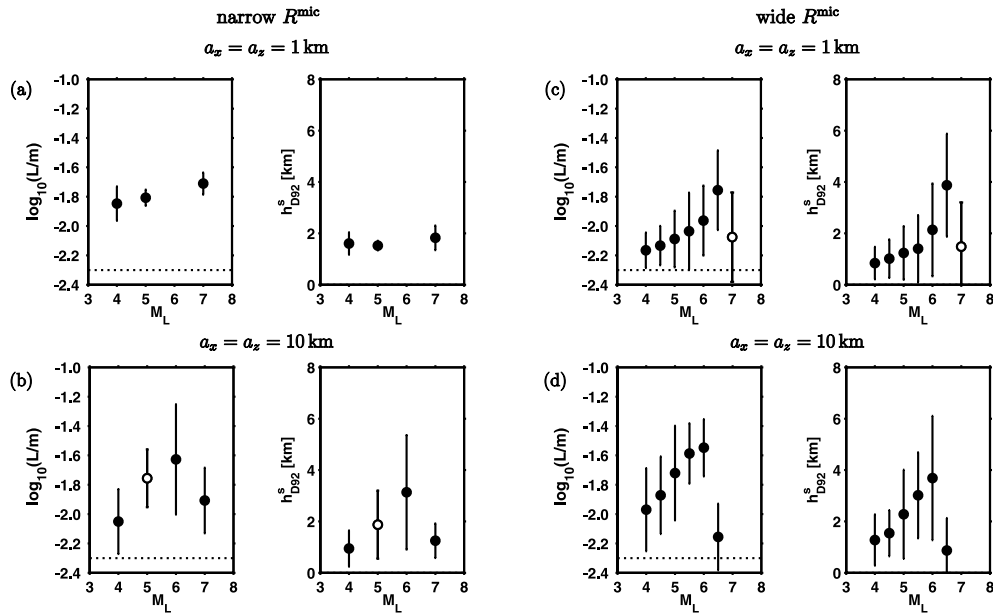
Figure 14. Collection of (bin-wide) averaged parameter values, L and h^s_{D92}, as a function of magnitude M_L, with (a) and (b) narrow R^{mic}, $M_I = 1$, (c) and (d) wide R^{mic}, $M_I = 0.5$. Solid circles represent data points with at least 10 events, open circles contain less than 10 events. Dotted lines denote L_{min}.

magnitude. Now we focus on relations between properties at the nucleation site and the magnitude of the event. This is of special interest since it is still an open question whether early stages of slip instability, which are assumed to be controlled by local conditions, scale with the final size of the earthquake. Before we discuss results from the bulk of simulations we look at the effect of different binning strategies. Fig. 13 and Table 3 illustrate the effect of variable binwidths or magnitude intervals, M_I, on the quality of inferred correlation. Figs 13(a), (c) and (e) show an example of a simulation generating few events (Model CL009, see Table 1), juxtaposed with an example producing many model earthquakes (Figs 13b, d and f, Model CL018). The results are split into two sets, one containing all datapoints (sampling threshold 1, open circles), while in the second average values containing at least 10 events were considered (solid circles). We determine the mean L value in each bin and its standard deviation, and fit the datapoints with a linear regression determining the slope, β, and the correlation coefficient, R^2. As displayed by Table 3, for model CL018 the correlation increases with increasing binwidth, M_I, due to the decrease in datapoints. This effect is more significant for the model with many events, leading to $R^2 = 0.6$ for $M_I = 0.2$, showing almost no correlation, to $R^2 = 0.97$ for $M_I = 1$, a positive correlation. For model CL009, the results are more ambiguous due to the lack of datapoints. The best correlation is found for narrow bins and a sampling threshold of 10 events, decreasing towards larger M_I. In general, we view results to be more expressive when mean magnitudes of at least 10 events are considered. Based on the presented examples we observe a positive correlation of the average $\log_{10}(L)$ value at HL with magnitude, noting that the exact quality of the fit depends on M_I.

7.2 Magnitude dependence

Fig. 14 shows example average parameter values as a function of magnitude M_L. For each of the model classes an example with short and large correlation lengths is shown. As discussed, medium L values occupy most parts of the fault plane when L_d is narrow (Fig. 2h).

This leads to less significant trends for short correlation lengths (Fig. 14a), but an increase of $\log_{10}(L)$ and h^s_{D92} values as a function of magnitude for $M_L < 7$ events, if a_x, $a_z \geq 5$. The increase in physical values determining the nucleation size is persistent for models with a wide R^{mic} (Figs 14c and d). As in Fig. 14(b), we observe a positive correlation between the L, h^s_{D92} value and the final size of the event for small and moderate earthquakes. The break in scaling for $M_L \geq 7$ events is also significant for all cases considered. These results confirm the general trend found by Hillers *et al.* (2006, their Fig. 14). The comparison of the positive relation between physical properties and M_L to the less pronounced relation
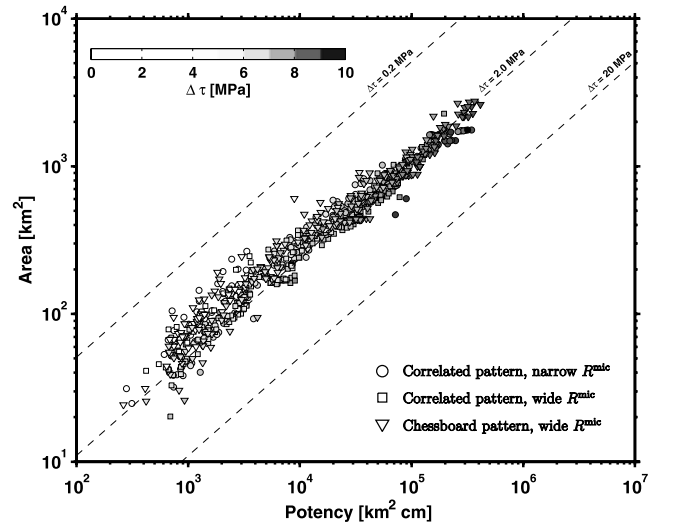

Figure 15. Standard area-size scaling for $M_L \geq 6$ events. Data are collected from 12 models, in particular from four models with narrow R^{mic}, four models with wide R^{mic} (Fig. 4), and four chessboard-type models from Hillers *et al.* (2006), respectively. The scaling relation suggest the overall self-similarity of earthquakes generated with models having 2-D L distributions with different statistical properties and topographies.

to χ, $d\chi$ (not shown) implies that local properties determine the hypocenter location more than evolving quantities. Most significant are the correlation values supporting an increase of $\log_{10}(L)$ and $h_{\mathrm{D92}}^{\mathrm{s}}$ at nucleation sites with increasing magnitude for $M_{\mathrm{L}} < 7$. Together with the breakdown of scaling at large events, this suggests a different scaling for nucleation of small/moderate and large earthquakes. Interestingly, the break of scaling at the transition between moderate and large events occurs approximately at the size where the vertical extension of earthquakes is saturated by the width of the seismogenic zone. At present we do not have an explanation for this break, but we speculate that differences in the initial stress drop may be responsible for this result. The result suggest that early deformation stages during accelerating slip are influenced by physical properties at the nucleation site. However, the large error bars in the present study indicate that the final size of the slip event is not exclusively controlled by nucleation properties. In agreement with Olson & Allen (2005), this implies that the nucleation phase may contain some information on the final size of the earthquake. The observed scaling is in contrast to Lapusta & Rice (2003), who simulated very similiar initial moment release rates for small and large events in their elastodynamic framework with homogeneous L values. It is also possible that both models agree, since we detect similar $\log_{10}(L)$ values at the hypocenters of small ($M_{\mathrm{L}} \leq 4.5$) and large events, but we can not resolve realistic moment rates here.

8 SCALING RELATIONS

We merge data from several simulations illustrating the applicability of the chosen approach to study statistical properties of synthetic seismicity. Fig. 15 shows a frequently plotted scaling relation using observable quantities compiled from generic slip maps (Fig. 15 in Hillers *et al.* (2006)) of $M_{\mathrm{L}} \geq 6$ events collected from models with small and large correlation lengths and narrow and wide R^{mic}, respectively. In addition, we include data from four chessboard models studied by Hillers *et al.* (2006) to demonstrate the statistical independence of particular model implementations. The effective area denotes the sum of cells that slipped during a model earthquake, and the potency is an integral measure of the seismic slip of events. The collapse of the data to a narrow zone reveals that the statistics of individual events are not dominated by the statistical distribution of size scales on the fault itself. Thus, $M_{\mathrm{L}} = 6.5$ events occurring on faults whose parameterization corresponds to mature and immature fault zones, respectively, can not be distinguished by their scaling properties. Hence, the presented approach produces overall self-similar earthquakes, suggesting its efficiency to generate model earthquakes with properties comparable to natural seismicity (Kanamori & Anderson 1975; Ben-Zion 2003). The realistic area-potency stress-drop dependencies indicate that the synthetic data set is suitable for detailed investigation of further scaling relations difficult to assess based on the available observed data. A more systematic analysis of the source scaling properties of model seismicity is given in Mai *et al.* (2006, in preparation).

9 DISCUSSION AND CONCLUSIONS

A number of laboratory and field observations and various theoretical frameworks indicate that faults evolve from geometrically-disordered structures in early deformation phases toward regularity and geometrical simplicity (Ben-Zion & Sammis 2003, and references therein). Tse & Rice (1986), Rice (1993), Ben-Zion & Rice (1997), and Lapusta *et al.* (2000) showed that continuum fault models with homogeneous or weakly heterogeneous rate-and-state frictional properties do not produce realistic seismic response. There have been claims that homogeneous models can produce realistic complexity as a generic outcome of inertial dynamics (e.g. Carlson *et al.* 1991, 1994; Shaw 1994). However, as shown by Cochard & Madariaga (1996), Rice & Ben-Zion (1996), Shaw & Rice (2000) and others, this occurs only with special types of constitutive laws, and special parameter ranges within these laws. See a detailed discussion of this topic in Ben-Zion (2001). The available results indicate collectively that the typical response of a smooth continuum fault does not have a broad event distribution, and that strong spatial heterogeneity is required in general to produce spatio-temporal non-uniform seismic behaviour. Geometrically discontinuous fault segments have been represented by discrete numerical elements in a variety of discrete models, capable of producing generic slip complexities over broad ranges of scales (e.g. Burridge & Knopoff 1967; Carlson & Langer 1989a,b; Bak *et al.* 1987, 1988; Bak & Tang 1989; Ito & Matsuzaki 1990; Lomnitz-Adler 1993; Ben-Zion 1996; Zöller *et al.* 2005a,b; Dahmen *et al.* 1998). The inherent discreteness in those models allows the elements to fail independently in small slip events, while cascades of failures of a number of elements represent moderate and large earthquakes. The present study combines essential features of previous investigations suitable for the study of realistic seismicity within the continuum class of models. The planar representation of the fault is an efficient design to perform numerical experiments with a suitable resolution in space and time. The treatment of the problem in the continuum limit eliminates the grid size dependency of the inherently discrete models. The use of non-uniform spatial distributions of the critical rate-and-state slip distance L allows a controlled parameterization of imposed geometrical heterogeneity. A more general treatment will also account for effects of the heterogeneities on the normal stress. However, this is not done at the present modelling level.

We performed a systematic parameter space study to investigate the importance of the effective range of size scales—composed of micro- and macro-scopic attributes of the distribution of strength heterogeneities—on seismicity patterns associated with fault zones at different evolutionary stages. Models with variable R^{mic}—parametrized by the effective range of L values on the fault—show significant differences in response types at short correlation lengths. The frequency size statistics, temporal seismicity evolution, temporal clustering and stress functions reveal that models with a narrow microscopic range of size scales associated with localized, mature fault zones like the San Andreas and the North Anatolian faults produce characteristic event type seismicity. In contrast, models with a wide microscopic range of size scales, expressing geometrical disorder related to fault zones at early deformation stages, generate seismicity patterns with a GR statistics over almost the entire magnitude range. At larger correlation lengths, the differences in response types become less pronounced, indicating the dominance of segmentation on controlling the seismicity evolution. Choosing the Hurst exponent to control the heterogeneity reproduces results from simulations where correlation lengths are variable. In particular, models using a small $\mathcal{H}$ (relatively heterogeneous 2-D L distributions) show a significant difference between response types of models with wide and narrow microscopic range of size scales. Lower degrees of spatial heterogeneity, i.e. large clusters of similar L values with dimension of the order of W, lead to similar results between wide/narrow R^{mic}, confirming the essential role of segmentation. Hybrid models with variable correlation lengths confirm that the microscopic range of size scales is the most effective tuning parameter of the seismic responses corresponding to fault zones at

different deformation stages. These results support the ealier inferences of Ben-Zion (1996), Ben-Zion *et al.* (2003a), Zöller *et al.* (2005b) and Hillers *et al.* (2006).

The investigation of earthquake nucleation on physical properties at hypocenter locations reveals that events tend to begin in regions of low L values. We observe a 'one over size scale' functional dependence of nucleation frequency. The correlation becomes less significant at large correlation lengths, supporting the interpretation that the governing mechanism is macroscopic (segmentation) and not details of the microscopic L value distribution. Due to the functional dependence of the nucleation size on L, the correlation of effective nucleation size with the number of hypocenters follows the same trend as the L correlation, whereas the dependence on seismic coupling indicates a tendency of nucleation in areas of large coupling coefficients. The normalized hypocenter dependence, taking into account the ratio of seismically slipped to total number of cells, illustrates the efficiency of the microscopic range of size scales to control seismicity.

For models having a wide R^{mic} and small a_x, approximating fault zones at early deformation stages, we observe a positive correlation between the magnitude and the L, h_{D92}^s values at hypocenter location. This trend is observable for small and moderate earthquakes, and we find a clear break in scaling for large events (Pacheco *et al.* 1992), indicating that the nucleation process may be different for seismicity with $M_L \leq 6$ and large earthquakes. This suggest that early deformation stages during accelerating slip are influenced by the properties of the nucleation site, in agreement with Olson & Allen (2005) and contrary to Lapusta & Rice (2003). Realistic area-potency stress-drop scaling relations for a collection of synthetic events generated by models using various realizations of parameters imply an overall self-similarity of model seismicity. In addition to other statistical properties similar to those of natural seismicity, the obtained scaling relations support the applicability of heterogeneous 2-D L distributions in a continuum model to parametrize fault zone heterogeneity. Although some aspects of natural seismicity are shown to be reproduced, other important observations such as aftershock sequences are not generated by our simulations. Future studies with more sophisticated treatment of the rheology on a planar fault may be able to produce aftershock patterns.

ACKNOWLEDGMENTS

REFERENCES

Bak, P. & Tang, C., 1989. Earthquakes as a Self-Organized Critical Phenomenon, *J. geophys. Res.,* **94**(B11), 15 635–15 637.

Bak, P., Tang, C. & Wiesenfeld, K., 1987. Self-Organized Criticality: An Explanation of 1/f Noise, *Phys. Rev. Lett.,* **59**(4), 381–384.

Bak, P., Tang, C. & Wiesenfeld, K., 1988. Self-organized criticality, *Phys. Rev. A,* **38**(1), 364–374.

Ben-Zion, Y., 1996. Stress, slip, and earthquakes in models of complex single-fault systems incorporating brittle and creep deformations, *J. geophys. Res.,* **101**(B3), 5677–5706.

Ben-Zion, Y., 2001. Dynamic Rupture in Recent Models of Earthquake Faults, *J. Mech. Phys. Solids,* **49**, 2209–2244.

Ben-Zion, Y., 2003. Appendix 2, Key Formulas in Earthquake Seismology, in *International Handbook of Earthquake and Engineering Seismology, Part B,* pp. 1857–1875, eds Lee, W.H., Kanamori, H., Jennings, P.C. & Kisslinger, C., Academic Press.

Ben-Zion, Y. & Rice, J.R., 1995. Slip patterns and earthquake populations along different classes of faults in elastic solid, *J. geophys. Res.,* **100**(B7), 12 959–12 983.

Ben-Zion, Y. & Rice, J.R., 1997. Dynamic simulations of slip on a smooth fault in an elastic solid, *J. geophys. Res.,* **102**(B8), 17 771–17 784.

Ben-Zion, Y. & Sammis, C.G., 2003. Characterization of Fault Zones, *Pure appl. Geophys.,* **160**, 677–715.

Ben-Zion, Y. & Zhu, L., 2002. Potency-magnitude scaling relations for southern California earthquakes with $1.0 < M_L < 7.0$, *Geophys. J. Int.,* **148**, F1–F5.

Ben-Zion, Y., Eneva, M. & Liu, Y., 2003a. Large earthquake cycles and intermittend criticality on heterogeneous faults due to evolving stress and seismicity, *J. geophys. Res.,* **108**(B6), 2307, doi:10.1029/2002JB002121.

Ben-Zion, Y. *et al.*, 2003b. A shallow fault zone structure illuminated by trapped waves in the Karadere-Duzce branch of the North Anatolian Fault, western Turkey, *Geophys. J. Int.,* **152**, 699–717.

Blanpied, M.L., Lockner, D.A. & Byerlee, J.D., 1991. Fault stability inferred from granite sliding experiments at hydrothermal conditions, *Geophys. Res. Lett.,* **18**(4), 609–612.

Burridge, R. & Knopoff, L., 1967. Model and theoretical seismicity, *Bull. seism. Soc. Am.,* **57**(3), 341–371.

Carlson, J.M. & Langer, J.S., 1989a. Properties of Earthquakes Generated by Fault Dynamics, *Phys. Rev. Lett.,* **62**(22), 2632–2635.

Carlson, J.M. & Langer, J.S., 1989b. Mechanical model of an earthquake fault, *Phys. Rev. A,* **40**(11), 6470–6468.

Carlson, J.M., Langer, J.S., Shaw, B.E. & Tang, C., 1991. Intrinsic properties of a Burridge-Knopoff model of an earthquake fault, *Phys. Rev. A,* **44**(2), 884–897.

Carlson, J.M., Langer, J.S. & Shaw, B.E., 1994. Dynamics of earthquake faults, *Rev. Mod. Phys.,* **66**(2), 657–670, Colloquium Paper.

Chester, F.M. & Chester, J.S., 1998. Ultracataclasite Structure and Friction Processes of the Punchbowl Fault, San Andreas System, California, *Tectonophysics,* **295**, 199–221.

Cochard, A. & Madariaga, R., 1996. Complexity of seismicity due to highly rate-dependent friction, *J. geophys. Res.,* **105**(25), 25 891–25 907.

Dahmen, K., Ertas, D. & Ben-Zion, Y., 1998. Gutenberg-Richter and characteristic earthquake behavior in simple mean field models of heterogeneous faults, *Phys. Rev. E,* **58**(2), 1494–1501.

Dieterich, J.H., 1992. Earthquake nucleation on faults with rate- and state-dependent strength, *Tectonophysics,* **211**, 115–134.

Dieterich, J.H., 1994. A constitutive law for rate of earthquake production and its application to earthquake clustering, *J. geophys. Res.,* **99**(B2), 2601–2618.

Frohlich, C. & Davis, S.D., 1993. Teleseismic b values; or, much ado about 1.0, *J. geophys. Res.,* **98**, 631–644.

eds Hairer, E., Norsett, S.P.& Wanner, G., 1993. *Solving Ordinary Differential Equations I. Nonstiff Problems,* Springer, Berlin, 2nd edn.

Hillers, G., 2006. On the Origin of Earthquake Complexity in Continuum Fault Models With Rate and State Friction, Swiss Federal Institute of Technology, *PhD thesis,* Zurich (http://hdl.handle.net/2122/1024).

Hillers, G. & Miller, S.A., 2007. Dilatancy controlled spatio-temporal slip evolution of a sealed fault with spatial variations of the pore pressure, *Geophys. J. Int.,* **168**, 431–445.

Hillers, G., Ben-Zion, Y. & Mai, P.M., 2006. Seismicity on a fault with rate- and state-dependent friction and spatial variations of the critical slip distance, *J. geophys. Res.,* **111** (B01403), doi: 10.1029/2005JB003859.

Ito, K. & Matsuzaki, M., 1990. Earthquakes as Self-Organized Critical Phenomena, *J. geophys. Res.,* **95**(B5), 6853–6860.

Kanamori, H. & Anderson, D.L., 1975. Theoretical basis of some empirical relations in seismology, *Bull. seism. Soc. Am.,* **65**, 1073–1096.

Klein, J.B.R.W., 1993. Scaling and critical phenomena in a cellular automaton slider block model for earthquakes, *J. Stat. Phys.,* **72**, 405–412.

Lapusta, N. & Rice, J.R., 2003. Nucleation and early seismic propagation of small and large events in a crustal earthquake model, *J. geophys. Res.,* **108**(B4), 2205, doi: 10.1029/2001JB000793.

Lapusta, N., Rice, J.R., Ben-Zion, Y.& Zheng, G., 2000. Elastodynamic analysis for slow tectonic loading with spontaneous rupture episodes on faults with rate- and state-dependent friction, *J. geophys. Res.,* **105**(B10), 23 765–23 789.

Liu, Y. & Rice, J.R., 2005. Aseismic slip transients emerge spontaneously in three-dimensional rate and state modeling of subduction earthquake sequences, *J. geophys. Res.,* **110**, B08307, doi: 10.1029/2004JB003424.

Lomnitz-Adler, J., 1993. Automaton Models of Seismic Fracture: Constraints Imposed by the Magnitude-Frequency Relation, *J. geophys. Res.,* **98**(B10), 17 745–17 756.

Lyakhovsky, V., Ben-Zion, Y. & Agnon, A., 2001. Earthquake cycle, fault zones, and seismicity patterns in a rheologically layered lithosphere, *J. geophys. Res.,* **106**(B3), 4103–4120.

Mai, P.M. & Beroza, G., 2002. A spatial random field model to characterize complexity in earthquake slip, *J. geophys. Res.,* **107**(B11), 2308, doi:10.1029/2001JB000588.

Main, I., 1996. Statistical Physics, Seismogenesis, and Seismic Hazard, *Rev. Geophys.,* **34**(4), 433–462.

Marone, C., 1998. Laboratory-derived friction laws and their application to seismic faulting, *Annu. Rev. Earth Planet. Sci.,* **26**, 643–696.

Ohnaka, M., 2003. A constitutive scaling law and a unified comprehension for frictional slip failure, shear fracture of intact rock, and earthquake rupture, *J. geophys. Res.,* **108**(B2), 2080, doi: 10.1029/2000JB000123.

Olson, E.L. & Allen, R.M., 2005. The deterministic nature of earthquake rupture, *Nature,* **438**, 212–215.

Pacheco, J.F., Scholz, C.H. & Sykes, L.R., 1992. Changes in frequency-size relationship from small to large earthquakes, *Nature,* **355**, 71–73.

Pardo-Iguzquiza, E. & Chica-Olmo, M., 1993. The Fourier integral method: An efficient spectral method for simulation of random fields, *Math. Geol.,* **25**, 177–217.

Perfettini, H., Campillo, M. & Ionescu, I., 2003. On the scaling of the slip weakening rate of heterogeneous faults, *J. geophys. Res.,* **108**(B9), 2410, doi: 10.1029/2002JB001969.

Rice, J.R., 1993. Spatio-temporal Complexity of Slip on a Fault, *J. geophys. Res.,* **98**(B6), 9885–9907.

Rice, J.R. & Ben-Zion, Y., 1996. Slip complexity in earthquake fault models, *Proc. Natl. Acad. Sci. USA,* **93**, 3811–3818, Colloquium Paper.

Ruina, A., 1983. Slip Instability and State Variable Friction Laws, *J. geophys. Res.,* **88**(B12), 10 359–10 370.

Rubin, A.M. & Ampuero, J.-P., 2005. Earthquake nucleation on (aging) rate and state faults, *J. geophys. Res.,* **110** (B11312), doi:10.1029/2005JB003686.

Schorlemmer, D., Gerstenberger, M.C., Wiemer, S. & Jackson, D., 2006. Earthquake likelihood model testing, *Seism. Res. Lett.,* in press.

Shaw, B.E., 1994. Complexity in a spatially uniform continuum fault model, *Geophys. Res. Lett.,* **21**(18), 1983–1986.

Shaw, B.E. & Rice, J.R., 2000. Existence of continuum complexity in the elastodynamics of repeated fault ruptures, *J. geophys. Res.,* **105**(B10), 23 791–23 810.

Stirling, M.W., Wesnousky, S.G. & Shimazaki, K., 1996. Fault Trace Complexity, Cumulative Slip, and the Shape of the Magnitude-frequency Distribution for Strike-slip Faults: A Global Survey, *Geophys. J. Int.,* **124**, 833–868.

Stuart, W.D. & Tullis, T.E., 1995. Fault model for preseismic deformation at Parkfield, California, *J. geophys. Res.,* **100**, 24 079–24 099.

Sylvester, A.G., 1988. Strike-Slip Faults, *Geol. Soc. Am. Bull.,* **100**, 1666–1703.

Tchalenko, J.S., 1970. Similarities between shear zones of different magnitudes, *Geol. Soc. Am. Bull.,* **81**, 1625–1640.

Tse, S.T. & Rice, J.R., 1986. Crustal Earthquake Instability in Relation to the Depth Variation of Frictional Slip Properties, *J. geophys. Res.,* **91**(B9), 9452–9472.

Tullis, T.E., 1996. Rock friction and its implications for earthquake prediction examined via models of Parkfield earthquakes, *Proc. Natl. Acad. Sci. USA,* **93**, 3803–3810, Colloquium Paper.

Wesnousky, S.G., 1994. The Gutenberg-Richter or Characteristic Earthquake Distribution, Which Is It?, *Bull. seism. Soc. Am.,* **84**(6), 1940–1959.

Woessner, J., Schorlemmer, D., Wiemer, S. & Mai, P.M., 2006. Spatial correlation of aftershock locations and on-fault main shock properties, *J. geophys. Res.,* **111**, B08301, doi: 10.1029/2005JB003961.

Zöller, G., Hainzl, S., Hohlschneider, M. & Ben-Zion, Y., 2005a. Aftershocks resulting from creeping sections in a heterogeneous fault, *Geophys. Res. Lett.,* **32**, L03308, doi: 10.1029/2004GL021871.

Zöller, G., Hohlschneider, M. & Ben-Zion, Y., 2005b. The role of heterogeneities as a tuning parameter of earthquake dynamics, *Pure appl. Geophys.,* **162**, 1027–1049.

APPENDIX A: REVISITING NUCLEATION PROPERTIES

Nucleation Size Earthquake nucleation is the stage that precedes fast slip and rupture propagation. We give here a brief review of aspects of nucleation under rate-and-state friction that are relevant to our analysis of hypocenter locations, with emphasis on the length scales involved. Dieterich (1992) characterized the nucleation process by two stages: an early phase where slip localizes into a small region, followed by slip acceleration without lateral expansion. Based on the effective linear slip-weakening behaviour of the aging version of rate-and-state friction high above steady state, where healing can be neglected, and on 2-D quasi-static simulations of the nucleation process of single events (no cycles) with non-uniform initial conditions and friction properties, Dieterich (1992) proposed the following expression for the minimal size of the nucleation zone:

$$h_{\mathrm{D92}}^{\mathrm{n}} = \xi' \cdot L_b \qquad (A1)$$

where

$$L_b = \frac{GL}{b\,\sigma_{\mathrm{e}}}. \qquad (A2)$$

The factor $\xi' = 2.5$ results from the relation between stiffness and length scale and generally depends on geometry and boundary conditions. Rubin & Ampuero (2005) revisited in detail the nucleation problem and showed that the minimum localization length follows eq. (A1) with $\xi' = 2.75$. This length differs by a factor $(1 - a/b)\,\xi'/\xi$ from the length h_{R93}^{n}, defined in eq. (4), which was derived by a linear stability analysis with respect to uniform steady sliding (Ruina 1983). For an appropriate description of the nucleation process, $h_{\mathrm{D92}}^{\mathrm{n}}$ must be well resolved by the numerical discretization. If $a/b > 1 - \xi/\xi'$, this imposes more stringent requirements on the numerical cell size than the often cited criterion based on h_{R93}^{n}. The values used in this work lead to $h_{\mathrm{D92}}^{\mathrm{n}} = 435$ m and $h_{R93}^{\mathrm{n}} = 768$ m where $L = L_{\mathrm{min}}$.

For typical laboratory values of a/b, including the value $a/b = 0.79$ of the present study, Rubin & Ampuero (2005) found a different nucleation regime. After slip localization, the nucleation zone expands quasi-statically, analogous to subcritical crack growth, and tends to a larger final size at which slip rate accelerates to the dynamic range. Based on classical energy concepts in fracture mechanics they showed that the final nucleation size may be as large as

$$h_{\mathrm{RA05}}^{\mathrm{n}} \approx \frac{2L_b}{\pi} \cdot \left(\frac{b}{b-a} \right)^2. \qquad (A3)$$

In the simulations summarized in fig. 8 of Rubin & Ampuero (2005), the size of the region of dominant slip-rate when 'dynamic' slip-rates (≈ 1 m s^{-1}) are first reached is $1/2\,h_{\mathrm{RA05}}^{\mathrm{n}} \approx 8\,L_b$ if $a/b = 0.8$. This is a natural scale to consider for the analysis of hypocenter
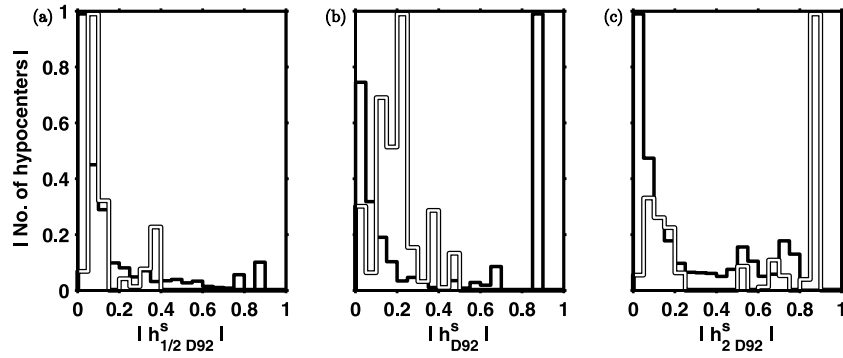
Figure 16. Correlations of the number of hypocenters on effective nucleation size, dependent on potentially smaller (a) and larger (c) nucleation sizes, h^n, with respect to the standard h^n_{D92} estimate (b) (*cf.* Fig. 11b). The smaller the assumed nucleation size, the better the correlation between small values and the number of nucleation sites.

locations. Here, $h^n_{RA05} = 2268\,\text{m}$ with $L = L_{min}$. However, h^n_{RA05} was originally defined for an infinitely long fault with uniform friction parameters driven by slow load. The different conditions of our study might affect nucleation in a number of ways. Strong heterogeneities of available stress drops (resulting from the earthquake cycle) or effective fracture energy (proportional to L), can limit the late expansion stage of nucleation. In regions of short L constrained to a size smaller than h^n_{RA05} by regions of larger L, dynamic events can be stopped prematurely. Moreover, slip rate can reach the dynamic range on scales smaller than h^n_{RA05} if there is a fast and strong stress trigger from a neighbouring event (see Rice 1993, for a similar comment).

Given these uncertainties, we explore the effect of potentially smaller and larger nucleation sizes by calculating additional maps of effective nucleation sizes, h^s, based on alternative nucleation sizes, $1/2\,h^n_{D92}$ and $2h^n_{D92}$, respectively. (Note that the smoothing algorithm does not allow the linear transformation $h^s_{D92} = f(h^n_{D92}) \rightarrow 1/2\,h^s_{D92} = f(h^n_{1/2\,D92})$.) The results shown in Fig. 16 explore the quality of the correlation between hypocenters and nucleation size at hypocenter locations. Fig. 16(b) illustrates the original estimate (Fig. 11a), whereas Figs 16(a) and (c) account for smaller and larger estimates, respectively. We observe a better correlation between small h^s values and the hypocenter for smaller original h^n estimates. However, this result depends on the definition of the hypocenter and its determination in a 3-D continuum model with heterogeneous L distributions, as discussed next.

Nucleation Sites In the present study we define the hypocenter to be the location of the accelerating cell that first becomes larger

than a certain threshold velocity. To be consistent with seismological observations it would be appropriate to define a dynamic event by a threshold in potency rate instead of a maximum slip rate. However, our quasi-dynamic simulations do not generate realistic potency rates or slip rates. Because we aim to compare the present results to those from previous work (Hillers *et al.* 2006) we choose a threshold velocity to define a seismic event. The 2-D analysis of Rubin & Ampuero (2005) provides an alternative estimate for hypocenter locations. Since nucleation takes the form of an expanding quasi-static crack, with slip rate concentrations at its edges, the dynamic threshold (of our definition) may not be reached at the center of the nucleation zone but at one at the edges. This implies that the hypocenter should be in the center of the accelerating centroid. To compare our definition with the centroid estimate, we compute at the time of nucleation, t_{nuc}, the x and z component of the velocity centroid C_x and C_z, respectively,

$$C_x(t_{nuc}) = \frac{1}{p(t_{nuc})} \sum_x x\, v(x, z, t_{nuc})$$

$$C_z(t_{nuc}) = \frac{1}{p(t_{nuc})} \sum_z z\, v(x, z, t_{nuc}), \tag{A4}$$

where $p(t_{nuc})$ is the potency rate. However, we find that the current approach produces a velocity contrast between aseismic sliding and quasi-dynamic seismic regimes which is not pronounced enough to use eq. (A4) as an alternative approach.